The Astrophysical Journal, 998:239 (23pp), 2026 February 20 https://doi.org/10.3847/1538-4357/ae3b2a

JADES: Rest-frame UV-to-NIR Size Evolution of Massive Quiescent Galaxies from Redshift $z = 5$ to $z = 0.5$

Zhiyuan Ji[1], Christina C. Williams[1,2], Katherine A. Suess[3,4], Sandro Tacchella[5,6], Benjamin D. Johnson[7], Brant Robertson[3], Stacey Alberts[1], William M. Baker[5,6], Stefi Baum[8], Rachana Bhatawdekar[9], Nina Bonaventura[1], Kristan Boyett[10,11], Andrew J. Bunker[12], Stefano Carniani[13], Stephane Charlot[14], Zuyi Chen[1], Jacopo Chevallard[12], Emma Curtis-Lake[15], Francesco D'Eugenio[5,6], Anna de Graaff[16], Christa DeCoursey[1], Eiichi Egami[1], Daniel J. Eisenstein[7], Kevin Hainline[1], Ryan Hausen[17], Jakob M. Helton[1], Tobias J. Looser[5,6], Jianwei Lyu[1], Roberto Maiolino[5,6,18], Michael V. Maseda[19], Erica Nelson[20], George Rieke[21], Marcia Rieke[1], Hans-Walter Rix[16], Lester Sandles[5,6], Fengwu Sun[1], Hannah Übler[5,6,22], Christopher N. A. Willmer[1], Chris Willott[23], and Joris Witstok[5,6]

[1] Steward Observatory, University of Arizona, 933 N. Cherry Avenue, Tucson, AZ 85721, USA; zhiyuanji@arizona.edu
[2] NSF's National Optical-Infrared Astronomy Research Laboratory, 950 N. Cherry Avenue, Tucson, AZ 85719, USA
[3] Department of Astronomy and Astrophysics, University of California, Santa Cruz, 1156 High Street, Santa Cruz, CA 95064, USA
[4] Kavli Institute for Particle Astrophysics and Cosmology and Department of Physics, Stanford University, Stanford, CA 94305, USA
[5] Kavli Institute for Cosmology, University of Cambridge, Madingley Road, Cambridge, CB3 0HA, UK
[6] Cavendish Laboratory, University of Cambridge, 19 JJ Thomson Avenue, Cambridge, CB3 0HE, UK
[7] Center for Astrophysics | Harvard & Smithsonian, 60 Garden Street, Cambridge MA 02138, USA
[8] Department of Physics and Astronomy, University of Manitoba, Winnipeg, MB R3T 2N2, Canada
[9] European Space Agency (ESA), European Space Astronomy Centre (ESAC), Camino Bajo del Castillo s/n, 28692, Villanueva de la Cañada, Madrid, Spain
[10] School of Physics, University of Melbourne, Parkville 3010, VIC, Australia
[11] ARC Centre of Excellence for All Sky Astrophysics in 3 Dimensions (ASTRO 3D), Australia
[12] Department of Physics, University of Oxford, Denys Wilkinson Building, Keble Road, Oxford OX1 3RH, UK
[13] Scuola Normale Superiore, Piazza dei Cavalieri 7, I-56126 Pisa, Italy
[14] Sorbonne Université, CNRS, UMR 7095, Institut d'Astrophysique de Paris, 98 bis bd Arago, 75014 Paris, France
[15] Centre for Astrophysics Research, Department of Physics, Astronomy and Mathematics, University of Hertfordshire, Hatfield AL10 9AB, UK
[16] Max-Planck-Institut für Astronomie, Königstuhl 17, D-69117, Heidelberg, Germany
[17] Department of Physics and Astronomy, The Johns Hopkins University, 3400 N. Charles Street, Baltimore, MD 21218, USA
[18] Department of Physics and Astronomy, University College London, Gower Street, London WC1E 6BT, UK
[19] Department of Astronomy, University of Wisconsin-Madison, 475 N. Charter Street, Madison, WI 53706, USA
[20] Department for Astrophysical and Planetary Science, University of Colorado, Boulder, CO 80309, USA
[21] Steward Observatory and Dept of Planetary Sciences, University of Arizona, 933 N. Cherry Avenue Tucson AZ 85721, USA
[22] Max-Planck-Institut für extraterrestrische Physik, Gießenbachstraße 1, 85748 Garching, Germany
[23] NRC Herzberg, 5071 West Saanich Road, Victoria, BC V9E 2E7, Canada
Received 2024 January 1; revised 2025 December 16; accepted 2026 January 16; published 2026 February 13

Abstract

We present the UV-to-near-IR (NIR) size evolution of a sample of 161 quiescent galaxies with $M_* > 10^{10}\,M_\odot$over $0.5 < z < 5$. With deep multiband NIRCam images in GOODS-South from JADES, we measure the effective radii (R_e) of the galaxies at rest-frame 0.3, 0.5, and 1 μm. On average, we find that quiescent galaxies are 45% (15%) more compact at rest-frame 1 μm than they are at 0.3 μm (0.5 μm). Regardless of wavelengths, the R_e of quiescent galaxies strongly evolves with redshift, and this evolution depends on stellar mass. For lower-mass quiescent galaxies with $M_* = 10^{10}$–$10^{10.6}\,M_\odot$, the evolution follows $R_e \propto (1+z)^{-1.1}$, whereas it becomes steeper, following $R_e \propto (1+z)^{-1.7}$, for higher-mass quiescent galaxies with $M_* > 10^{10.6}\,M_\odot$. To constrain the physical mechanisms driving the apparent size evolution, we study the relationship between R_e and the formation redshift ($z_{\rm form}$) of quiescent galaxies. For lower-mass quiescent galaxies, this relationship is broadly consistent with $R_e \propto (1+z_{\rm form})^{-1}$, in line with the expectation of the progenitor effect. For higher-mass quiescent galaxies, the relationship between R_e and $z_{\rm form}$ depends on stellar age. Older quiescent galaxies have a steeper relationship between R_e and $z_{\rm form}$ than that expected from the progenitor effect alone, suggesting that mergers and/or post-quenching continuous gas accretion drive additional size growth in very massive systems. We find that the $z > 3$ quiescent galaxies in our sample are very compact, with mass surface densities $\Sigma_e \gtrsim 10^{10}\,M_\odot\,{\rm kpc}^{-2}$, and their R_e are possibly even smaller than anticipated from the size evolution measured for lower-redshift quiescent galaxies. Finally, we take a close look at the structure of GS-9209, one of the earliest confirmed massive quiescent galaxies at $z_{\rm spec} \sim 4.7$. From UV to NIR, GS-9209 becomes increasingly compact, and its light profile becomes more spheroidal, showing that the color gradient is already present in this earliest massive quiescent galaxy.

Unified Astronomy Thesaurus concepts: Galaxy formation (595); Galaxy evolution (594); Galaxy structure (622); High-redshift galaxies (734)

1. Introduction

The origin and evolution of massive and quiescent galaxies that no longer form stars are major open questions in astrophysics. The last two decades of research have revealed that massive quiescent galaxies emerge rapidly, but in small numbers, at least as early as $z \gtrsim 4$. By $z < 1$, such galaxies dominate the total stellar mass budget of the Universe (e.g., O. Ilbert et al. 2013; A. Muzzin et al. 2013). Understanding their evolutionary history is thus a critical piece of building a coherent picture of cosmic evolution.

Galaxy sizes encode information about the spatial distribution of different components within galaxies, including stellar populations, dust, and gas, and how these components evolve. Because size evolution is influenced by both internal processes, such as star formation and feedback, and external ones, such as interactions and mergers, it provides an integrated record of the mechanisms that assemble and transform galaxies.

The near-infrared (NIR) cameras on the Hubble Space Telescope (HST) enabled measurement of the rest-optical structure of massive galaxies up to $z \sim 2.5$. A key revelation was the extremely compact morphology of quiescent galaxies at Cosmic Noon: They are five times smaller on average at $z \sim$ 1–2 compared to their presumed descendants at $z \sim 0$ (E. Daddi et al. 2005; S. Toft et al. 2007; I. Trujillo et al. 2007; P. G. van Dokkum et al. 2008; I. Damjanov et al. 2011; A. B. Newman et al. 2012, to name a few), and their stellar mass densities rival the densest stellar structures known in the Universe (e.g., P. F. Hopkins et al. 2010b). In addition, compared to star-forming galaxies of similar mass and redshift, quiescent galaxies display more dramatic evolution in size from $z \sim 2.5$ to the present (e.g., S. Shen et al. 2003; A. van der Wel et al. 2014; G. Barro et al. 2017). Which processes are driving this strong size evolution of quiescent galaxies, and whether the dominant processes change over time have sparked contentious debate. It is expected for galaxies to increase in size over time given the Λ cold dark matter (CDM) cosmology, because cosmic mass density decreases over time due to the expansion of the Universe, and galaxy size should, to some extent, reflect the density of the Universe at its formation epoch, i.e., the progenitor effect (e.g., P. J. E. Peebles 1993; H. Mo et al. 2010; S. J. Lilly & C. M. Carollo 2016). Disentangling whether the size increase toward lower redshifts is due to the progenitor effect, or that the galaxies themselves increase in size without appreciable increase in mass (e.g., through gas-poor minor mergers) has been a key target of numerous studies (e.g., R. Bezanson et al. 2009; P. F. Hopkins et al. 2009; T. Naab et al. 2009; L. Fan et al. 2010; P. G. van Dokkum et al. 2010; A. B. Newman et al. 2012; L. Oser et al. 2012; P. Cassata et al. 2013; C. C. Williams et al. 2017; K. A. Suess et al. 2019a; Z. Ji & M. Giavalisco 2022).

How the structure of quiescent galaxies evolves in earlier times—at $z > 2.5$—still eludes us. At this redshift range, HST is limited to the wavelengths of rest-frame UV, i.e., blueward of 4000 Å. Likely because the rest-UV sizes are not representative of the true distributions of stellar mass in galaxies due to nonnegligible impact of color gradients (e.g., K. A. Suess et al. 2019a, 2019b; M. Mosleh et al. 2020; T. B. Miller et al. 2022), earlier studies relying on HST have found conflicting results. Some studies say that early quiescent-galaxy sizes are consistent with extrapolations from lower-redshift quiescent galaxies, while some argue that early quiescent galaxies are exceedingly compact (C. M. S. Straatman et al. 2015; M. Kubo et al. 2018; P. Lustig et al. 2021). Obviously, in the HST era, the major limitation preventing a complete picture was the lack of deep and high-resolution rest-frame optical/NIR imaging at $z > 2.5$, which prevented both robust photometric characterization due to large uncertainties in spectral energy distribution (SED) modeling, and rest-frame optical morphologies.

The recent launch of JWST (J. P. Gardner et al. 2023) has opened a new window to view early quiescent galaxies in exquisite detail. Its unprecedented sensitivity and wavelength sampling enable more robust modeling of stellar populations and star formation history (SFH) reconstruction. The arrival of Cycle 1 JWST data demonstrated the power of this new facility to identify and characterize robust massive quiescent-galaxy candidates at $z > 2.5$, (A. C. Carnall et al. 2023a; F. Valentino et al. 2023) and make spectroscopic confirmations (T. Nanayakkara et al. 2022; A. C. Carnall et al. 2023b; K. Glazebrook et al. 2023) even as early as $z \sim 5$. Of particular importance to understanding their formation pathways, JWST, *for the first time*, now allows measurements of their rest-frame optical and NIR structures at high angular resolution and to higher redshifts than previously possible (out to $z \sim 10$, well beyond the limit of HST at $z \sim 2.5$).

A quantitative understanding of how quiescent galaxies grow in size across cosmic time is crucial, because structural evolution is directly linked to their formation pathways. The extremely compact morphologies and high stellar mass densities of early quiescent galaxies imply that they assembled their stars rapidly in dense environments, yet by the present day, quiescent systems have become significantly more extended in the local Universe. Distinguishing whether this apparent growth in size is dominated by the continuous addition of newly quenched, larger galaxies (progenitor effect), or by physical size increase of individual systems through minor mergers and dynamical processes, has fundamental implications for how galaxies quench and evolve. This work contributes to this effort by using ultra-deep HST and JWST imaging to measure the size of massive quiescent galaxies over $0.5 < z < 5$. The combination of high angular resolution, homogeneous SED fitting, and a mass-complete sample allows us to trace half-light radii at different rest-frame wavelengths with unprecedented precision.

Specifically, in this paper, we use the ultra-deep NIRCam imaging from the JWST Advanced Deep Extragalactic Survey (JADES; D. J. Eisenstein et al. 2023) to investigate the redshift evolution of the half-light sizes of quiescent galaxies, measured at rest-frame UV, optical, and NIR wavelengths. We focus in particular on massive galaxies with stellar mass $\log(M_*/M_\odot) > 10$, in order to focus on the formation pathways mostly independent of environmentally driven quenching, a process that affects primarily lower-mass galaxies (e.g., Y.-j. Peng et al. 2010; Z. Ji et al. 2018; C. Papovich et al. 2018). Throughout this paper, we adopt the AB magnitude system and the ΛCDM cosmology with Planck Collaboration et al. (2020) parameters, i.e., $\Omega_m = 0.315$ and $h = H_0/(100\,\mathrm{km\,s^{-1}\,Mpc^{-1}}) = 0.673$.

2. Observations

The sample of quiescent galaxies presented this work is in the GOODS-South (M. Giavalisco et al. 2004) portion of

JADES where we have obtained deep JWST/NIRCam imaging in nine filters, i.e., F090W, F115W, F150W, F200W, F277W, F335M, F356W, F410M, and F444W. At the time of writing, the JADES program is still ongoing, and the parts of observations (PID: 1180 and 1210) included in this study cover a total sky area of ≈ 60 arcmin^2, including regions around the Hubble Ultra-Deep Field where additional five medium-band NIRCam imaging observations, i.e., F182M, F210M, F430M, F460M, and F480M, have been obtained by the JWST Extragalactic Medium-band Survey (JEMS; C. C. Williams et al. 2023; PID: 1963).

We reduce all of these NIRCam imaging observations using a consistent method, which has been presented in detail in M. Rieke & the JADES Collaboration (2023). In short, we process the raw images using the JWST Calibration Pipeline with some custom corrections. Specifically, during the Stage 1 of the JWST pipeline, we mask and correct for the "snowballs" effect caused by charge deposition arising from cosmic-ray hits. During the Stage 2 of the JWST pipeline, we remove the $1/f$ noise and subtract 2D background from the images, and also correct the "wisp" features in the short-wavelength (i.e., filters bluer than F277W) images. Afterwards, we tie the astrometry of individual exposures of a given visit to the World Coordinate System (WCS) of a reference catalog constructed from HST Wide Field Camera 3 (WFC3) F160W mosaics in GOODS-South with astrometry tied to Gaia-EDR3 (Gaia Collaboration et al. 2021). Finally, we combine individual visit-level mosaics together to create the final mosaic, where we choose a pixel scale of 0.03 arcsec pixel^{-1} for all filters.

We also use the ancillary HST imaging observations taken from the latest Hubble Legacy Fields Data Release in GOODS-South (G. Illingworth et al. 2016; K. E. Whitaker et al. 2019), including the imaging data of the ACS/WFC F435W, F606W, F775W, F850LP, and F814W filters, and of the WFC3 F105W, F125W, F140W, and F160W filters. All of these HST images are on the same WCS grid as our NIRCam images.

The JADES photometry is measured using a customized pipeline based on PHOTUTILS (see M. Rieke & the JADES Collaboration 2023 for details). In brief, source detection was performed using a segmentation map generated from the stacked NIRCam LW image. All imaging data, from HST to NIRCam, were point-spread function (PSF)-matched by convolving and resampling each band to a common PSF defined at F444W (see Z. Ji et al. 2023 for details on reconstructing the JADES common PSF models). Fluxes were then measured from the PSF-homogenized mosaics using both segmentation-defined apertures (Kron, isophotal) and a set of circular apertures with different radii, with local background levels estimated and subtracted for each source. In our subsequent SED analysis (Section 4.1), we use the Kron fluxes, which provide the best global measurements of galaxy colors. Photometric uncertainties were calculated from the noise properties of the mosaics and propagated through the measurement process, following methods similar to those in I. Labbé et al. (2005) and R. Quadri et al. (2007).

3. Sample Selection

As the JADES program is still ongoing, the motivation of this work is *not* to test, improve, or develop selection methods to build a complete demographic picture of quiescent-galaxy populations across a wide dynamic range of stellar mass. Instead, we focus this paper only on the population of massive quiescent galaxies with stellar masses $M_* > 10^{10}\,M_\odot$. Because existing HST surveys are remarkably complete at this stellar-mass range (>90% complete; Y. Guo et al. 2013; Z. Ji et al. 2018; a detailed discussion regarding sample completeness can be found in Section 3.2), our strategy is to make full use of the power of those legacy surveys in GOODS-South to first select candidate galaxies using methods that have been extensively tested in the literature, and then refine the selected galaxies using SED fitting with our new JWST data.

3.1. Selecting Candidate Quiescent Galaxies Using *Rest*-UVJ Colors from 3D-HST

Our primary selection of quiescent galaxies is based on the redshift-dependent criteria of rest-frame *UVJ* colors (R. J. Williams et al. 2009). We take advantage of the measurements from the 3D-HST survey (G. B. Brammer et al. 2012; R. E. Skelton et al. 2014). We first impose a cut on the signal-to-noise ratio (S/N > 10) in the HST/F160W filter, which ensures high-quality photometry and, hence, those previous measurements of galaxy physical properties from 3D-HST. We then select galaxies with $M_* > 10^{9.7}\,M_\odot$[24] from the 3D-HST catalog. Finally, we use the rest-frame $(U-V)$ and $(V-J)$ colors from the 3D-HST catalog to make the initial selection of candidate quiescent galaxies.

We select candidate quiescent galaxies whose rest-frame colors satisfy the UVJ criteria from C. Schreiber et al. (2015):

$$\begin{aligned}(U-V) &> 1.3,\\ (V-J) &< 1.6,\\ (U-V) &> 0.88(V-J) + 0.49.\end{aligned} \quad (1)$$

We add to our analysis additional seven[25] $z > 2$ quiescent galaxies from A. C. Carnall et al. (2020), which appear in the JADES footprint. A. C. Carnall et al. (2020) made the selection of $M_* > 10^{10}\,M_\odot$ quiescent galaxies at $z > 2$ based on their refined SED modeling that allows for sufficiently flexible solutions over a wide range of observed redshifts and specific star formation rates (sSFR; see their Table 2). A. C. Carnall et al. (2020) showed that their selection is highly consistent with the *UVJ* technique, with an 80% overlapping fraction, but is more complete in that their SED modeling enabled the selection of relatively young quiescent galaxies that have bluer $(U-V)$ colors that would otherwise have been missed using the lower-redshift *UVJ* selection criteria.

The above selection gives us a total of 268 candidate massive quiescent galaxies at $z > 0.5$. We then remove galaxies hosting bright active galactic nuclei (AGNs) from our analysis, especially because the presence of AGNs can affect the interpretation of their morphological measures. We first remove X-ray AGNs by cross-matching the sample with the X-ray catalog from the 7Ms Chandra Deep Field South

[24] The SED-fitting code PROSPECTOR is elected to use in this work (Section 4.1). It has been noted that the stellar mass measures from PROSPECTOR are 0.1–0.3 dex higher (e.g., J. Leja et al. 2022; Z. Ji & M. Giavalisco 2022); therefore, we use this $10^{9.7}\,M_\odot$ cut to ensure our initial selection includes the vast majority of galaxies with $M_* \geqslant 10^{10}\,M_\odot$ from PROSPECTOR.

[25] The most galaxies from A. C. Carnall et al. (2020) have already been selected by the UVJ technique described above.

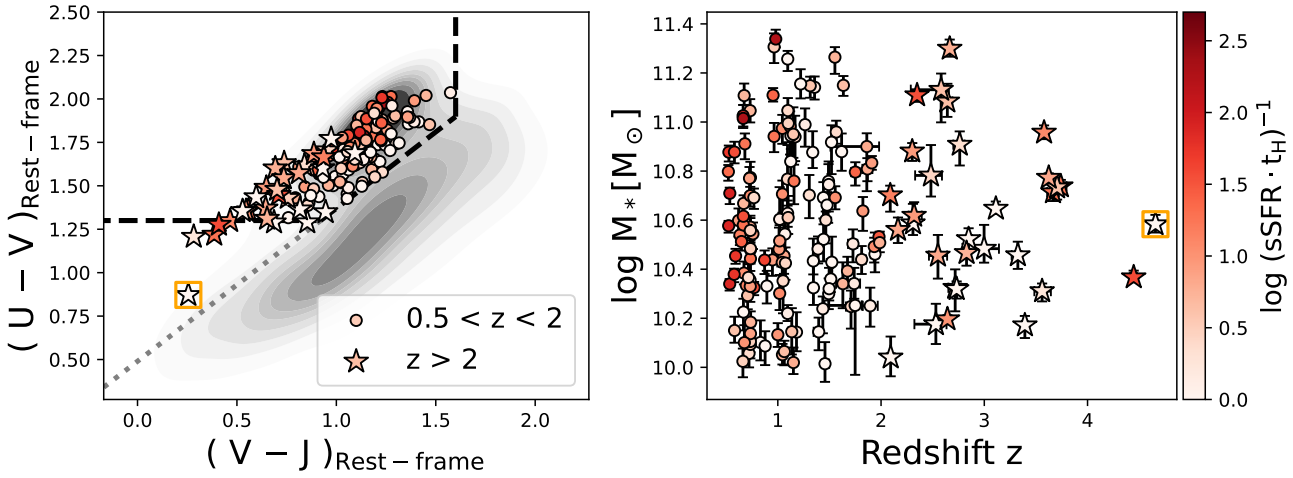

Figure 1. The final sample of 161 massive quiescent galaxies presented in this work (Section 3). Quiescent galaxies at $z > 2$ are shown as stars, while those at $0.5 < z < 2$ are shown as circles. The orange square marks the quiescent galaxy GS-9209 at $z_{\rm spec} = 4.658$ (A. C. Carnall et al. 2023b). Each one of the galaxies is color-coded according to its star formation intensity, quantified using $(\frac{1}{\rm sSFR})/t_{\rm H}$ (Section 3.2). Left panel: rest-frame *UVJ* color diagram. Background gray contours show the distribution of all galaxies with stellar mass $\log M_* > 10$ and redshift $0.5 < z < 5$ from 3D-HST. Black dashed lines show the criteria from C. Schreiber et al. (2015), which we use for the selection of quiescent galaxies at $z < 2$. Following recent studies, we relax the criterion of the horizontal cut on $(U - V)$ to select quiescent galaxies at $z \geqslant 2$ (Section 3). Right panel: the distribution of the quiescent-galaxy sample in the stellar mass-redshift space.

(B. Luo et al. 2017). We then remove IR AGNs using IRAC colors (J. L. Donley et al. 2012; Z. Ji et al. 2022). We also remove radio AGNs identified by the latest and deepest Very Large Array radio observations in GOODS-South (W. Rujopakarn et al. 2023, in preparation). Finally, we remove other types of AGNs identified by recent SED fitting from J. Lyu et al. (2022). Adding all of these different AGN types together, we identify a total of 71 AGN-hosting galaxies, corresponding to a fraction of 26% ± 4% (71/268), which is in broad agreement with that found in galaxies of similar masses at Cosmic Noon (e.g., Y. Q. Xue et al. 2010; Z. Ji et al. 2022). We mention that we retain the $z_{\rm spec} = 4.658$ quiescent galaxy GS-9209 that has recently been spectroscopically confirmed with the JWST/NIRSpec observation by A. C. Carnall et al. (2023b). This galaxy is not identified as an AGN based on the selection methods considered above, but it does host a faint AGN, as suggested by the broad Hα emission in the NIRSpec spectrum. However, because this AGN is so faint that its broadband size measurement—except for the morphology in F356W, which covers Hα (Section 6.2.2)—is not significantly biased by AGN contribution, we decide to keep this galaxy in the following analysis.

After removing the AGN-hosting galaxies, our initial selection based on 3D-HST measurements yields a sample of 197 candidate quiescent galaxies at $0.5 < z < 5$.

3.2. Finalizing the Quiescent Sample Using JADES Data

We note that the 3D-HST rest-frame colors were computed using EAzY, whose template sets are less comprehensive than those employed in a full SED-fitting framework. We therefore refine the rest-frame color measurements using SED fitting with the new photometry from JADES. We perform SED fitting with a total of more than 20-filter photometry from HST through JWST using the code PROSPECTOR (B. D. Johnson et al. 2021; see also Section 4.1 for details). We then use these newly obtained best-fit SEDs to re-measure the rest-frame *UVJ* colors. At $z < 2$, we retain the galaxies still satisfying all three UVJ color cuts (Equation (1)). At higher redshift ($z > 2$), most objects still lie within the conventional *UVJ* box; however, recent studies have shown that a subset of $z \gtrsim 2$ quiescent galaxies can fall just outside the traditional boundary, primarily due to slightly bluer $U - V$ colors (e.g., F. Valentino et al. 2023). This is generally interpreted as reflecting younger stellar ages at earlier cosmic times (K. E. Whitaker et al. 2013; S. Belli et al. 2019; A. C. Carnall et al. 2020). Motivated by these results, for $z > 2$ we adopt a slightly relaxed criterion by requiring galaxies to satisfy the diagonal color cut (the gray dotted line in Figure 1), following the recommendation of A. C. Carnall et al. (2020). We did not apply this relaxation in our initial selection because broadening the *UVJ* region can substantially increase contamination from star-forming galaxies (A. C. Carnall et al. 2020; F. Valentino et al. 2023). Mitigating this contamination typically requires additional cuts based on SFR or sSFR, which are challenging to constrain robustly for quiescent systems (see later discussion in this section). Since our primary goal is to measure the size evolution of quiescent galaxies, we prioritized sample purity in the selection; the relaxed $z > 2$ criterion would add only a small number of sources (<10% of the $z > 2$ sample; A. C. Carnall et al. 2020; also, see W. M. Baker et al. 2025b). Finally, we note that, as shown in Figure 1, only a few galaxies lie outside the conventional *UVJ* box. We verified that including or excluding them does not change any of our conclusions.

Our final sample consists of 161 robust *UVJ*-selected quiescent galaxies with $M_* > 10^{10}\,M_\odot$ at $0.5 < z < 5$, among which 130 and 31 galaxies are at $z < 2$ and $z \geqslant 2$, respectively. Among the 36 removed galaxies (i.e., 197–161), 18 were excluded because their stellar masses are $<10^{10} M_\odot$ based on our PROSPECTOR fits (note that our initial mass cut in the 3D-HST catalog is $10^{9.7} M_\odot$ to account for possible systematics in stellar-mass estimates; see Section 3.1). The remaining 18 galaxies were removed because their PROSPECTOR-derived *UVJ* colors fall outside the *UVJ* selection box. To investigate the origin of this discrepancy, we re-ran their SED fitting with PROSPECTOR using pre-JWST photometry and found that the vast majority (15/18) still lie outside the *UVJ* box. This shows that inaccurate *UVJ* colors from EAzY, likely

due to its limited template set, are the main reason for their misclassification.

Recent studies also used alternative selection methods of quiescent galaxies based on a fixed or redshift-dependent threshold of sSFR (e.g., J. S. Speagle et al. 2014; M. Donnari et al. 2019; J. Leja et al. 2022; S. Tacchella et al. 2022). However, accurately measuring sSFRs for quiescent galaxies with photometry only is challenging (C. Conroy 2013), which is highly sensitive to SED model assumptions (e.g., C. Pacifici et al. 2023). As the Appendix shows, we observe a significant systematic offset in the sSFR measures by simply changing SFHs (Section 4.1), meaning that whatever sSFR thresholds we use to select quiescent galaxies would be highly model-dependent. By contrast, the rest-frame *UVJ* color measures are largely insensitive to the SED model assumptions, making it a more empirical way to select quiescent galaxies. Because of this, we choose to still use the *UVJ* technique in this work. Nevertheless, the *UVJ* selection is highly consistent with the selection methods based on sSFR. To show this, in the left panel of Figure 1 we plot the distribution of our final quiescent sample in the rest-frame *UVJ* diagram. We color code each one of the galaxies according to $(\frac{1}{\mathrm{sSFR}})/t_{\mathrm{H}}$, i.e., the ratio of the mass doubling time at the current star formation rate[26] to the Hubble time at the time of observation. A larger $(\frac{1}{\mathrm{sSFR}})/t_{\mathrm{H}}$ corresponds to a lower star formation intensity. Regardless of SFH assumptions (see the Appendix), we find that the UVJ-selected quiescent galaxies have longer mass doubling time than the Hubble time, confirming that the UVJ-selected quiescent galaxies also have low sSFRs.

The final quiescent sample obtained here is highly mass complete at $z > 3$. J. Leja et al. (2020) estimated the 100% mass-complete limit for the full 3D-HST survey to be $\sim 10^{10.1} M_{\odot}$ at $z \sim 3$ (see their Figure 1). The GOODS-S region considered in this work is deeper than the other 3D-HST fields by ∼0.2–0.5 mag in HST/F160W, implying that our adopted mass threshold of $10^{10} M_{\odot}$ is safely about the 100% mass completeness limit. In addition, massive quiescent galaxies at high redshift are intrinsically bright: at $z > 2.5$, our galaxies span F444W = 21–24 AB, comparable to NIRCam-identified quiescent systems at similar redshifts (e.g., W. M. Baker et al. 2025b), and more than 5 magnitudes brighter than the 5σ limit of JADES (M. Rieke & the JADES Collaboration 2023). These magnitudes are also >1 mag brighter than the pre-JWST IRAC depths in GOODS-S (∼25 AB; R. E. Skelton et al. 2014), meaning that all galaxies already had robust IRAC detections with high signal-to-noise (S/N $\gtrsim$ 10 in both Channel 1 and Channel 2). Previous template-fitting analyses of IRAC photometry in GOODS-S demonstrated excellent consistency among deblending methods at these bright magnitudes (Y. Guo et al. 2013), indicating that rest-frame UVJ colors were already well constrained for these galaxies in the pre-JWST imaging.

Independent indications further support the high completeness of the sample at $z > 3$. The number densities of massive quiescent galaxies derived from our sample are fully consistent with those inferred in other JWST legacy fields within uncertainties (W. M. Baker et al. 2025a), suggesting that no significant population is missed in our selection. Moreover, using the recently released JADES SED-fitting catalog (C. Simmonds et al. 2025), we verify that all galaxies at $3 < z < 5$ with $\log(M/M_{\odot}) > 10$ and $\log(\mathrm{sSFR}/\mathrm{yr}^{-1}) < -11$ are present in our final sample. Altogether, these lines of evidence demonstrate that the quiescent sample presented here is highly complete down to $10^{10} M_{\odot}$ over $0.5 < z < 5$. Any residual incompleteness, if present, is expected to be negligible and should not significantly affect any of the conclusions reached in this work.

4. Measurements

4.1. SED Fitting with Prospector

With the JADES photometry that samples the wavelength range from rest-frame UV to NIR with more than 20 filters, we perform SED fitting using the code Prospector (B. D. Johnson et al. 2021), with the emphasis on robustly measuring stellar mass, photometric redshift, and sSFR. We assume a similar SED model used in Z. Ji et al. (2023). In brief, we adopt the FSPS stellar synthesis code (C. Conroy et al. 2009; C. Conroy & J. E. Gunn 2010) with the stellar isochrone libraries MIST (J. Choi et al. 2016; A. Dotter 2016) and the stellar spectral libraries MILES (J. Falcón-Barroso et al. 2011). We adopt the P. Madau (1995) intergalactic medium absorption model and include the nebular emission model of N. Byler et al. (2017). We model the dust attenuation following S. Tacchella et al. (2022) where the dust attenuation of nebular emission and young stellar populations, and of old stellar populations, is treated differently (S. Charlot & S. M. Fall 2000). We fix the redshift when a spectroscopic one is available;[27] otherwise, we fit it as a free parameter with a flat prior of $z \in (0.1, 10)$.

As the fiducial model of this study, we assume nonparametric, piece-wise SFH composed of nine lookback time bins, where SFR is constant within each bin. We model nonparametric SFH using the Dirichlet prior (J. Leja et al. 2017), which can recover high-fidelity SFHs of different galaxy types while effectively mitigating the overfitting problem (J. Leja et al. 2019). In addition, this prior has been demonstrated, with synthetic observations from cosmological simulations, to give the unbiased inference of stellar ages for massive quiescent galaxies at $z \sim 2$ (see Appendix A in Z. Ji & M. Giavalisco 2022).

In Figure 2 we compare the redshifts and stellar masses from our Prospector fitting with those from 3D-HST (G. B. Brammer et al. 2012; R. E. Skelton et al. 2014). The agreement between the redshift measures is excellent. Our Prospector measurement of stellar masses is also tightly correlated with that from 3D-HST, although our stellar masses are systematically higher by ≈0.16 dex, a quantitatively similar systematics has also been found by other studies (e.g., J. Leja et al. 2019; S. Lower et al. 2020; Z. Ji & M. Giavalisco 2022; J. Leja et al. 2022; Z. Ji & M. Giavalisco 2023). In the Appendix, we further test our measurements with another two different SFHs, namely nonparametric SFHs with the continuity prior (J. Leja et al. 2019) and delayed-tau parametric SFHs. We show that our measurements of stellar mass, rest-frame UVJ colors (hence, the selection of quiescent galaxies) are robust.

[26] Here the current star formation rate is defined as the star formation rate of the first lookback time bin, i.e., 0−30 Myr, from our fiducial SED fitting (Section 4.1).

[27] We use the spectroscopic redshift catalog in GOODS-South compiled by the ASTRODEEP project (E. Merlin et al. 2021).

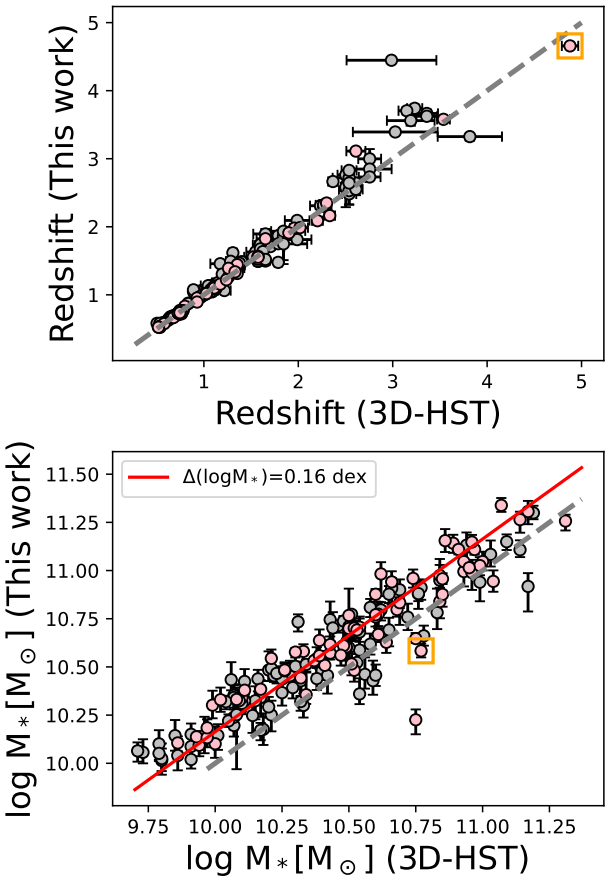

Figure 2. Comparisons of the redshift (top panel) and stellar-mass (bottom panel) measures. Galaxies with spectroscopically confirmed redshifts are color-coded in pink. GS-9209 is marked with the orange square. The gray, dashed line marks the one-to-one relationship. The uncertainty of photometric redshifts from our PROSPECTOR fitting is smaller than the point and, hence, hard to see in the plot. Our stellar-mass measures with PROSPECTOR are systematically higher by 0.16 dex relative to the measures from 3D-HST.

4.2. Measuring Rest-frame Sizes

In this paper we refer to the circularized effective (half-light) radius ($R_e = R_{e,\rm maj} \times \sqrt{b/a}$) as the size of galaxies.[28] We measure the size at three characteristic rest-frame wavelengths—0.3, 0.5, and 1 μm—using different wide-band images. As Figure 3 illustrates, we can perform the most measurements using NIRCam images from JADES, except the rest-0.3 μm sizes for galaxies at $z < 1.3$, which we instead use the HST/ACS F606W images. We have tested our results by linearly interpolating[29] the measurements of two adjacent filters to get the size at the exact rest-frame wavelength. We found no substantial changes in any of our conclusions.

We measure the size by performing PSF-convolved morphological fitting using the software GALFIT (version 3.0.5; C. Y. Peng et al. 2010), where each one of the galaxies is modeled as a single 2D Sérsic profile. Before running GALFIT, we first center on each one of the galaxies to make a $7'' \times 7''$ cutout. Similar to previous studies (e.g., A. van der Wel et al. 2012), we only allow the Sérsic index n to vary between 0.2 and 8. To mitigate possible impacts from adjacent galaxies on

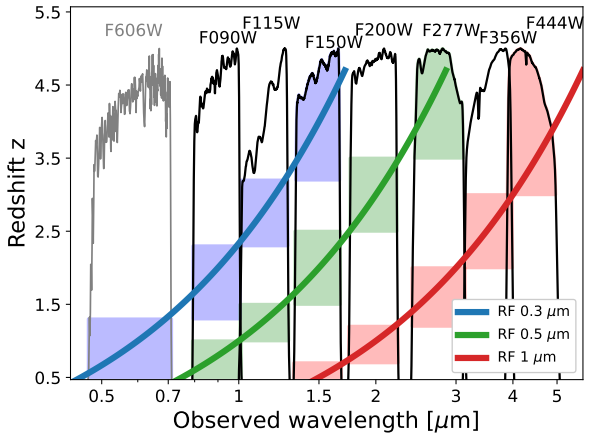

Figure 3. Wide-band filters used for the rest-frame 0.3 μm (blue), 0.5 μm (green), and 1 μm (red) size measures. Except for the HST/ACS F606W, all other filters are from JWST/NIRCam.

the morphological fitting, we use the JADES segmentation map (M. Rieke & the JADES Collaboration 2023) to mask out all neighboring galaxies in the cutouts. By default, we fit the local sky background of each cutout as a free parameter. The PSFs used for the fitting are the model PSFs (mPSFs) of JADES (Z. Ji et al. 2023). The mPSFs are generated using the software WEBBPSF (v1.1.1; M. D. Perrin et al. 2014), where we have carefully taken into account the effect of data reduction. As demonstrated by Z. Ji et al. (2023; see their Appendix A), the mPSFs are highly consistent with the commonly used effective PSFs (ePSFs; J. Anderson & I. R. King 2000) to the level of $\approx$1% in terms of enclosed energy radial profiles. The biggest advantage of using mPSFs, especially for the extragalactic deep fields like JADES, which contain a very limited number of bright, unsaturated isolated stars in their footprints, is that it allows us to have robust, stable PSF models to larger ($>1''$) angular scales.

We estimate uncertainties of the fitted parameters using a Monte Carlo method. Specifically, we use the error flux extension of the NIRCam data to Monte Carlo resample the image pixel values 300 times. We then run GALFIT on the resampled images and use the range between 16th and 84th percentiles as 1σ uncertainties. In this paper, because we only focus on massive galaxies that are detected with S/N > 100 in the JWST images,[30] the derived uncertainty of R_e is generally very small. For reference, we find a median uncertainty of NIRCam/F150W size to be $\delta R_e/R_e \approx 2\%$, which is in quantitative agreement with the uncertainties estimated for galaxies with similar S/Ns using HST/F160W images (see Figure 6 in A. van der Wel et al. 2012, and Figure 6 in Z. Ji et al. 2022).

We now test systematics of our GALFIT fitting. First, we consider the systematics introduced by the local sky background estimation. Instead of fitting the sky as a free parameter, if we fix it to the 3σ-clipped median pixel value of the cutout after masking out all detected sources using the segmentation map, the median relative difference in the size measures will be $\approx$1%. Second, instead of using mPSFs, if we use ePSFs in the GALFIT fitting, the median relative difference in the size measures will be $\approx$3%. These systematic uncertainties are small and have no impacts on the results of

[28] We find no substantial changes in our conclusions if we use the effective semimajor axis instead.

[29] For the two $z > 4$ galaxies in our sample, we actually need do the extrapolation to get their rest-frame 1 μm sizes.

[30] For the galaxies presented in this paper, the median S/N is 220 in F150W, and is 450 in F444W, where S/N is measured within the Kron aperture.

Table 1
Median Sizes of Massive Quiescent Galaxies and Their Best-fit Evolution with Redshift

	$z = 0.5 \sim 1.0$	$z = 1.0 \sim 1.5$	$z = 1.5 \sim 2.0$	$z = 2.0 \sim 2.5$	$z = 2.5 \sim 5.0$	β[a]	C[a]
$R_e(0.3\ \mu m)$[b]	$2.11^{+0.52}_{-0.33}$	$1.39^{+0.26}_{-0.22}$	$1.47^{+0.21}_{-0.31}$	$0.94^{+0.43}_{-0.08}$	$0.56^{+0.19}_{-0.07}$	$-1.23^{+0.21}_{-0.24}$	$0.62^{+0.10}_{-0.11}$
$R_e(0.5\ \mu m)$[b]	$1.90^{+0.17}_{-0.26}$	$1.30^{+0.16}_{-0.13}$	$1.07^{+0.17}_{-0.14}$	$0.72^{+0.42}_{-0.06}$	$0.60^{+0.11}_{-0.21}$	$-1.24^{+0.21}_{-0.17}$	$0.57^{+0.07}_{-0.08}$
$R_e(1.0\ \mu m)$[b]	$1.55^{+0.17}_{-0.20}$	$1.10^{+0.13}_{-0.13}$	$0.96^{+0.19}_{-0.09}$	$0.6^{+0.07}_{-0.05}$	$0.38^{+0.17}_{-0.04}$	$-1.33^{+0.19}_{-0.18}$	$0.53^{+0.06}_{-0.07}$

Notes. [†]Values shown in the table are the medians and their 1σ uncertainties from our bootstrap Monte Carlo method (Section 5.2).
[a] The best-fit relation of $\log R_e = \beta \log(1+z) + C$.
[b] In units of kiloparsecs.

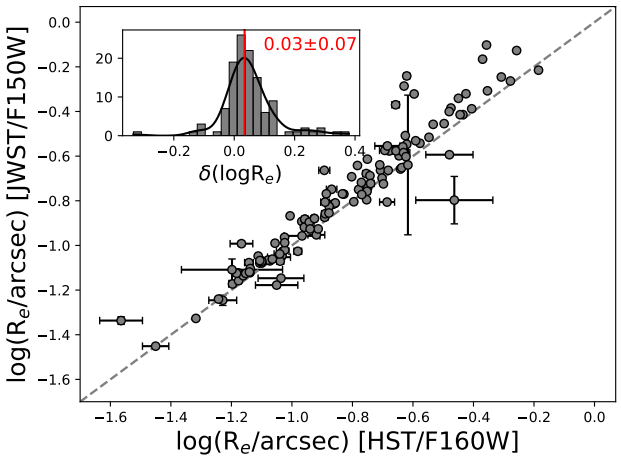

Figure 4. Size from our measurements using the NIRCam/F150W images (y-axis; Section 4.2) as a function of size from A. van der Wel et al. (2012), who performed the measurements using the HST/WFC3 F160W images (x-axis). The agreement between the two measurements is great, with a median difference ($y - x$) of 0.03 dex and a standard deviation of 0.07 dex.

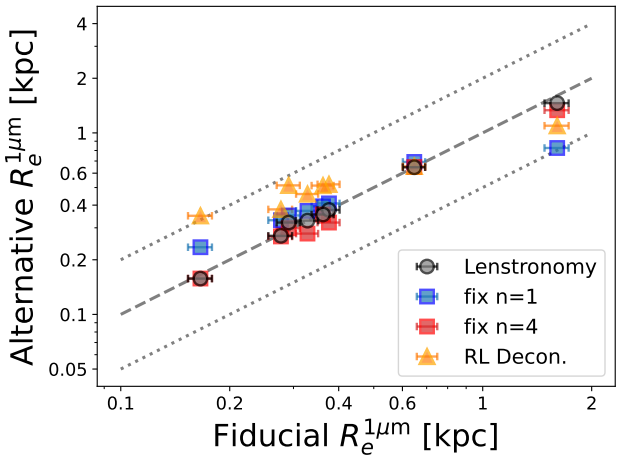

Figure 5. Rest-frame 1 μm sizes of the $z > 3$ quiescent galaxies from different methods. The x-axis shows the fiducial measurements in this work (Section 4.2). The y-axis shows the measurements from alternative methods detailed in Section 4.2.1, including using (1) a different morphological fitting tool LENSTRONOMY (black circles), (2) GALFIT but fixing Sérsic index $n = 1$ (blue squares) or $n = 4$ (red squares) during the fit, and (3) a nonparametric method with the Richardson–Lucy deconvolution (orange triangles). The main purpose here is to compare the sizes from different methodologies, we thus do not estimate uncertainties for the y-axis. The dashed line marks the one-to-one relation, and the dotted lines mark the 2 times above/below the one-to-one relation. For the vast majority of the $z > 3$ quiescent galaxies, the relative difference in sizes from different methods is <50%.

this work. Finally, we compare our NIRCam/F150W sizes to the HST/WFC3 F160W sizes measured by A. van der Wel et al. (2012). As Figure 4 shows, we find excellent agreement between the two measures, with a median difference of 0.03 ± 0.07 dex. Moreover, among the 161 quiescent galaxies, we find that 24 F150W GALFIT fits hit the Sérsic index bounds ($n = 0.2$ or 8), which is also consistent with A. van der Wel et al. (2012), who found 21 F160W fits having the same issue.

We remove galaxies with $n = 0.2$ or 8 from our sample to ensure reliable size measures for the size evolution analysis. Specifically, we remove 37, 25, and 25 galaxies from the analysis of the rest-frame 0.3 μm, 0.5 μm, and 1 μm size evolution, respectively. We note that all of the removed fits have $n = 8$, indicating that those galaxies have very compact cores. Removing them from our analysis thus can drag the median size up. To check the magnitude of this impact, for the galaxies with unreliable single-Sérsic fits, we use the alternative approach with the Richardson–Lucy deconvolution algorithm (see Section 4.2.1 below for details) to estimate their sizes, and then add these alternative sizes back to the analysis. Despite that the best-fit parameters of the size evolution are consistent with those reported in Table 1 within uncertainty, the intercept C (Equation (3)) systematically reduces by 0.08, 0.06, and 0.05 dex for rest-frame 0.3 μm, 0.5 μm, and 1 μm sizes, respectively. Other than this, we find no substantial changes in any of our results.

4.2.1. Testing the Size Measures for the z > 3 Galaxies

As we will show in Section 5.2, the $z > 3$ quiescent galaxies in our sample have typical sizes of $R_e^{1\ \mu m} \sim 0.3$ kpc, corresponding to $0\farcs04$ at $z = 3$, which is only slightly larger than the $0\farcs03$ pixel scale of JADES mosaics. Moreover, all of the $z > 3$ quiescent galaxies have large Sérsic indices $n > 2$. Long tails of large Sérsic index profiles can make the analysis sensitive to profile mismatch and sky background estimates (C. Y. Peng et al. 2010). We thus conduct several further tests to check the robustness of the rest-frame 1 μm size estimates for these extremely compact galaxies at $z > 3$.

First, the robustness of Sérsic fitting, especially for galaxies with very compact morphologies, relies on accurate pixelization and integration of Sérsic profiles. As shown by A. S. G. Robotham et al. (2017; see their Figure 7), the flux-weighted error model image generated by GALFIT increases with Sérsic n. We thus test our Sérsic fitting for the $z > 3$ quiescent galaxies with LENSTRONOMY (K. Suess et al. 2026, in preparation), a newly developed morphological fitting code that adopts new algorithms to generate Sérsic models and to conduct fitting. We plot the results as black circles in Figure 5.

Excellent agreement is seen between the sizes from GALFIT and from LENSTRONOMY.

Second, the degeneracy between R_e and Sérsic n (e.g., Z. Ji et al. 2020, 2022) makes the size measures uncertain. To check how sensitive the size estimates are due to uncertain n, instead of fitting n as a free parameter, we run GALFIT by fixing $n = 1$ (exponential disk) or $n = 4$ (de Vaucouleurs profile) for the $z > 3$ quiescent galaxies. In Figure 5, the results are shown as blue and red squares, respectively. The sizes from the $n = 4$ Sérsic fitting are in very good agreement with our fiducial measurements, which is expected, since all of the galaxies have $n > 2$ from the default Sérsic fitting. The agreement between the fiducial sizes and those from the $n = 1$ fitting is also good, with the differences well within a factor of 2. We note that, relative to our default Sérsic fitting, the reduced χ^2 increases by factors of 1.8 and 1.1 for the fitting with fixed $n = 1$ and $n = 4$, respectively, showing that the quality of fitting is better with n as a free parameter, as expected.

Third, it is known that the light profile of quiescent galaxies can be more complex than a single-Sérsic profile (e.g., S. Huang et al. 2013a, 2013b). R. Davari et al. (2014) simulated quiescent galaxies at different redshifts by mimicking their light profiles using the detailed substructures observed in nearby elliptical galaxies. They found that the systematic uncertainty of the size measures at $z \sim 2$ from single-Sérsic fitting is at the level of ~10%–20%. If high-redshift quiescent galaxies indeed have similarly multicomponent light profiles like lower-redshift counterparts, the tests done by R. Davari et al. (2014) will then suggest that the mismatch of assumed light profiles only introduces subtle bias in the inferred sizes. However, because the rest-frame NIR light distribution of quiescent galaxies at $z > 3$ remains largely unknown, we further test our size measures using the nonparametric approach with the Richardson–Lucy deconvolution algorithm (W. H. Richardson 1972). In brief, Richardson–Lucy deconvolution is an iterative method for recovering an estimate of a source's intrinsic image given an observed image blurred by a known PSF. It assumes the image formation is essentially observed $\approx$ true * PSF, and updates the current estimate of the "true" image by comparing (pixel-by-pixel) the observed image to a PSF-blurred version of the current estimate. The update is multiplicative and is derived as a maximum-likelihood solution under Poisson noise, which naturally enforces nonnegative flux. With more iterations, it can sharpen structure.

With precise PSF models, images can be restored to some accuracy through the iterative Richardson–Lucy algorithm. As a sanity check, we run Richardson–Lucy deconvolution for the mPSF image (Section 4.2) of F444W, i.e., the filter used for the rest-1 μm size measures at $z > 3$ (Figure 3). After ~50 iterations, the FWHM of the deconvolved mPSF image asymptotes to $0\farcs015$, i.e., half the pixel size, which is the theoretical limit we can achieve for JADES images with the Richardson–Lucy deconvolution, showing the effectiveness of this technique. Thus, our strategy is to first deconvolve the F444W images of the $z > 3$ quiescent galaxies, and then directly estimate the effective radii ($R_e^{\rm RL\dagger}$) of the galaxies by measuring their radial light profiles in the deconvolved images. In this way, the PSF effect can be largely mitigated, and the difference between $R_e^{\rm RL\dagger}$ of the galaxies and that of the PSF, i.e., $0\farcs015$, can be considered as a result of the intrinsic broadening due to the sizes of the galaxies. The sizes can then be inferred following

$$R_e^{\rm RL}[\rm arcsec] = \sqrt{(R_e^{\rm RL\dagger})^2 - (0.015)^2}\,, \quad (2)$$

where $R_e^{\rm RL\dagger}$ is the half-light radius measured directly from the deconvolved image using the photometric curve of growth computed with circular apertures.

The biggest advantage of the method above based on the Richardson–Lucy deconvolution is that it does not require an assumed form for the parametric light profile, and any complex structures in the galaxies are naturally taken into account during the $R_e^{\rm RL}$ estimates. Moreover, this method does not bias toward brighter parts of the galaxies (which differs from GALFIT, which conducts χ^2 minimization fitting and hence essentially provides light-weighted measures). The disadvantage of this method, though, is that no formal stop criterion exists for the iterative process (M. Prato et al. 2012), as such image deconvolution is mathematically ill-posed. Previous HST studies by A. van der Wel et al. (2011) fixed the number of iterations to be 16. In our cases, we find that, once the iteration number is >10, the $R_e^{\rm RL}$ measures become very stable for the $z > 3$ quiescent galaxies.

In Figure 5, $R_e^{\rm RL}$ are shown as orange triangles (based on 50 times Richardson–Lucy iterations). We have visually inspected the deconvolved image for each galaxy and found no clear artifacts introduced by the Richardson–Lucy deconvolution process. Even with this very different approach, we still find very good agreement with the sizes derived from the default single-Sérsic fitting with GALFIT. We also note that, despite the $z > 3$ quiescent galaxies being very compact, our analysis based on the Richardson–Lucy deconvolution suggests that their light profiles are inconsistent with point sources, as all of them have $R_e^{\rm RL\dagger} > 0\farcs015$; i.e., the galaxies are (marginally) resolved in F444W.

Finally, we stress that the purpose of running different tests here is not to evaluate which methodology is the best in characterizing the morphology of high-redshift quiescent galaxies. In principle, one could use simulated galaxies with assumed light profiles to compare the performance of different size-measurement techniques. However, the scientific usefulness of such tests is fundamentally limited for the present study, because the detailed light distributions of quiescent galaxies at $z > 3$ remain poorly constrained. Any simulation-based conclusions would therefore depend on likely over-simplified assumptions about the intrinsic light profiles, which may not capture the true structural diversity of these systems. As a result, such tests could have limited interpretive value and may even introduce misleading biases rather than clarifying the robustness of the measurements. Instead, our goal is to check if the size estimates of the $z > 3$ quiescent galaxies suffer from any significant systematic uncertainties from the imperfect fitting algorithm, the degeneracy between R_e and n, and the mismatch of assumed light profiles. Regardless of methods, we find strong correlations between the sizes from our fiducial measurements and the sizes from other alternative methods described above. The differences in sizes from different methods are well within a factor of 2. In fact, the relative difference in size is <50% for the vast majority of the $z > 3$ galaxies (Figure 5). We thus conclude that the size estimates for the quiescent galaxies at $z > 3$ in our sample are not sensitive to significant systematic uncertainties; hence, the strong size evolution of quiescent galaxies toward $z > 3$ reported below (Section 5.2) is robust.

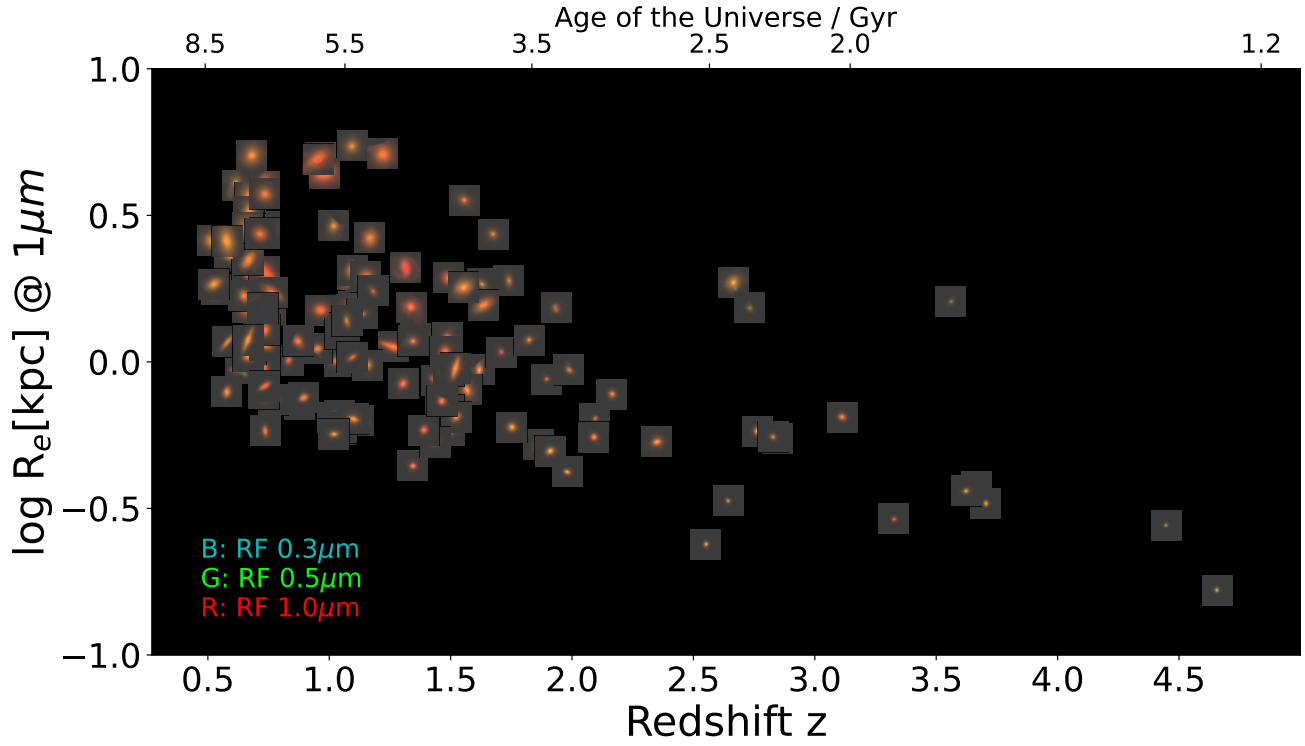

Figure 6. RGB cutouts of massive quiescent galaxies presented in this work. Each one of the galaxies is plotted at its location in the diagram of rest-frame 1 μm size evolution. The filters used to produce the RGB cutouts are illustrated in Figure 3. The size of the cutouts is 20 kpc × 20 kpc.

5. Results

Figure 6 presents the RGB images of individual quiescent galaxies in this work, where the RGB filters are chosen to probe rest-frame 0.3, 0.5, and 1.0 μm (Figure 3) and each galaxy is plotted at the corresponding location in the diagram of rest-1 μm size versus redshift. We observe strong size evolution of quiescent galaxies from $z \sim 5$ to $z \sim 0.5$. In what follows, we will quantify and compare the size evolution at different rest-frame wavelengths from UV through NIR. We will also explore the possible dependence of size evolution on the physical properties of quiescent galaxies. Finally, we will present the stellar mass–size relationship of massive quiescent galaxies.

5.1. Multiwavelength Sizes: Piecing Together the Physical Drivers of Size Evolution

Because of the spatial variations of dust attenuation and stellar-population properties, galaxies show radial gradients of stellar mass-to-light ratio, which makes the interpretation of the apparent evolution of projected light profiles nontrivial (e.g., K. A. Suess et al. 2019a, 2019b; M. Mosleh et al. 2020; T. B. Miller et al. 2022; A. van der Wel et al. 2023). In this work, we perform the morphological analysis at three different wavelengths—that are sensitive to different physical processes—to constrain the physical drivers of the size evolution of quiescent galaxies. The two shorter wavelengths are chosen to be rest-frame 0.3 and 0.5 μm, which cover key stellar-population features around the rest-frame 4000 Å region. The third characteristic wavelength is chosen to be rest-frame 1 μm, which is a sensitive probe of stellar-mass distributions, and is the longest wavelength where we can still measure galaxy morphology with the JADES NIRCam imaging over the redshift range considered here (Figure 3).

Compared to rest-UV and optical, rest-NIR light profiles are a much better proxy for the stellar-mass distribution of galaxies, because the stellar mass-to-light ratio at NIR only weakly, if at all, depends on recent star formation (e.g., E. F. Bell & R. S. de Jong 2001; S. S. McGaugh & J. M. Schombert 2014). To show this, we cross match our quiescent sample with the catalog from K. A. Suess et al. (2020) who measured galaxy half-mass sizes ($R_{\rm halfmass}$) using HST data based on spatially resolved SED fitting. A total of 116 galaxies in our sample have the $R_{\rm halfmass}$ measures. In the top panel of Figure 7, we plot $R_{\rm halfmass}$ as a function of R_e measured at different wavelengths. Strong correlations are observed between $R_{\rm halfmass}$ and R_e, regardless of which wavelength R_e is measured. Systematic offsets are also observed between $R_{\rm halfmass}$ and R_e, likely due to the different methodologies used for the size measures.

We compare the agreement between $R_{\rm halfmass}$ and R_e measured at different wavelengths. In the bottom panel of Figure 7, we show the histograms of Δ, the relative difference between $R_{\rm halfmass}$ and R_e. We measure the standard deviation of Δ, i.e., $\sigma(\Delta)$. We estimate the uncertainty of $\sigma(\Delta)$ through a bootstrap Monte Carlo method. Specifically, we bootstrap the sample, use normal distributions to Monte Carlo resample the values of $R_{\rm halfmass}$ and R_e with the corresponding measurement uncertainties, and finally, we measure $\sigma(\Delta)$. We repeat the procedure 1000 times and use the range between 16th and 84th percentiles as the uncertainty of $\sigma(\Delta)$. As the inset of the bottom panel of Figure 7 shows, the Δ between $R_{\rm halfmass}$ and $R_e^{1\ \mu{\rm m}}$ has the smallest scatter, showing rest-NIR light profiles indeed a robust, much better proxy for stellar-mass distributions than the rest-UV and optical ones.

In what follows, we thus will use $R_e^{1\ \mu{\rm m}}$ as the size proxy for stellar-mass distributions of the galaxies. Because the 4000 Å break contains key information related to dust attenuation,

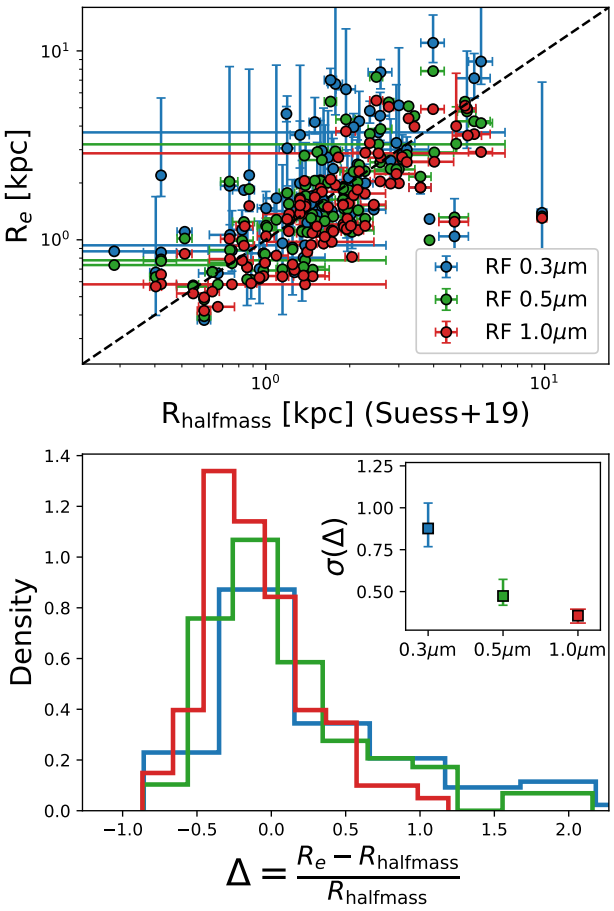

Figure 7. Half-light sizes R_e vs. half-mass sizes $R_{halfmass}$ for the subsample of quiescent galaxies whose $R_{halfmass}$ measures are available from K. A. Suess et al. (2019b). Rest-frame 0.3, 0.5, and 1 μm R_e are shown in blue, green, and red, respectively. The bottom panel shows histograms of the difference between the half-light and half-mass sizes (Δ), and the inset shows the standard deviation of Δ (Section 5.2). The agreement between $R_{halfmass}$ and rest-1 μm R_e is the best.

stellar age, and metallicity, combining with the size evolution at rest-frame 0.3 and 0.5 μm, we will be able to empirically constrain the physical mechanisms driving the size evolution of quiescent galaxies.

5.2. Size Evolution of Quiescent Galaxies from UV–NIR

We characterize the size evolution by fitting the relationship between the R_e and z of individual quiescent galaxies with a functional form of

$$\log R_e = \beta \log(1 + z) + C. \quad (3)$$

To estimate the uncertainties of β and C, we bootstrap the entire sample, use normal distributions to Monte Carlo resample the size and redshift measures with the corresponding uncertainties, and finally fit the size evolution. We repeat this bootstrap Monte Carlo procedure 1000 times and use the range between the 16th and 84th percentiles as 1σ uncertainties. The best-fit relationships are present in Table 1 and Figure 8.

5.2.1. The Pace of the Size Evolution

Regardless of rest-frame wavelengths, the size of quiescent galaxies evolves with redshift at a similar pace, i.e., a similar $\beta \approx -1.25 \pm 0.20$ (Table 1). Because the fitting of size evolution was done using the measurements of individual galaxies and most of the quiescent galaxies in our sample are at $z < 2$, the low-redshift quiescent galaxies have more weight in the fitting procedure.[31] Notwithstanding the very limited sample size at $z > 3$, by looking at the bottom panels of Figure 8, we note that the vast majority of $z > 3$ quiescent galaxies are below (i.e., have smaller sizes than) the best-fit R_e–z relationship. To better show this, we estimate the median sizes of quiescent galaxies at different redshifts. We divide the entire sample into five redshift bins, i.e., four bins between $z = 0.5$ and $z = 2.5$ with an interval of $\Delta z = 0.5$ and the last bin of $z > 2.5$. Similarly, we use the bootstrap Monte Carlo method to estimate the uncertainties of the median sizes. As the top-left panel of Figure 8 shows, the median size of the highest-redshift bins deviates from the best-fit size evolution—quiescent galaxies at $z > 3$ are smaller than the predictions by extrapolating the size evolution of lower-z quiescent galaxies. We will discuss the implications regarding this finding later in Section 6.2.

We continue to divide the sample into two mass bins using the median stellar mass $\langle \log(M_*/M_\odot) \rangle = 10.6$. We present the size evolution of the two mass bins in Figure 9 and Table 2. We observe a dependence of the size evolution on stellar mass, where the evolution is faster—more negative β (Equation (3))—for more-massive quiescent galaxies. This finding does not depend on the rest-frame wavelength at which the sizes are measured (Table 2).

We further check the robustness of this stellar-mass dependence. Considering the relatively small sample size of this study (161 galaxies), instead of dividing the sample into more stellar mass bins, we first sort stellar masses of individual quiescent galaxies into an increasing order. Then, starting from the first 30 of the sorted sample, we keep adding more-massive quiescent galaxies into the fit of size evolution. We finally study the change of β as a function of the maximum stellar mass of quiescent galaxies included in the fit. As Figure 10 shows, β becomes increasingly negative as more massive quiescent galaxies are included, confirming that the size evolution is faster for more-massive quiescent galaxies. In Section 6.1, we will discuss in detail the implications of this finding for the physical mechanisms governing the size evolution of massive quiescent galaxies.

5.2.2. The Difference in Size at Different Wavelengths

The intercept C (Equation (3)) of the size evolution depends on rest-frame wavelengths (Figure 8). Massive quiescent galaxies are larger at shorter wavelengths: relative to their rest-1 μm sizes, on average, quiescent galaxies are larger by 45% at rest-frame 0.3 μm and 15% at rest-frame 0.5 μm. Our results are in quantitative agreement with other recent JWST studies (K. A. Suess et al. 2022; A. van der Wel et al. 2023), showing that the stellar-mass distribution of quiescent galaxies is significantly more compact than their rest-frame UV and optical light distributions, caused by the radial changes in stellar-population properties such as stellar age, metallicity, and dust attenuation (e.g., K. A. Suess et al. 2022; T. B. Miller et al. 2023; A. van der Wel et al. 2023; K. A. Suess et al. 2023).

[31] We verified that the fitted parameters change only subtly when we fit the size evolution using only the $z < 3$ galaxies in our sample.

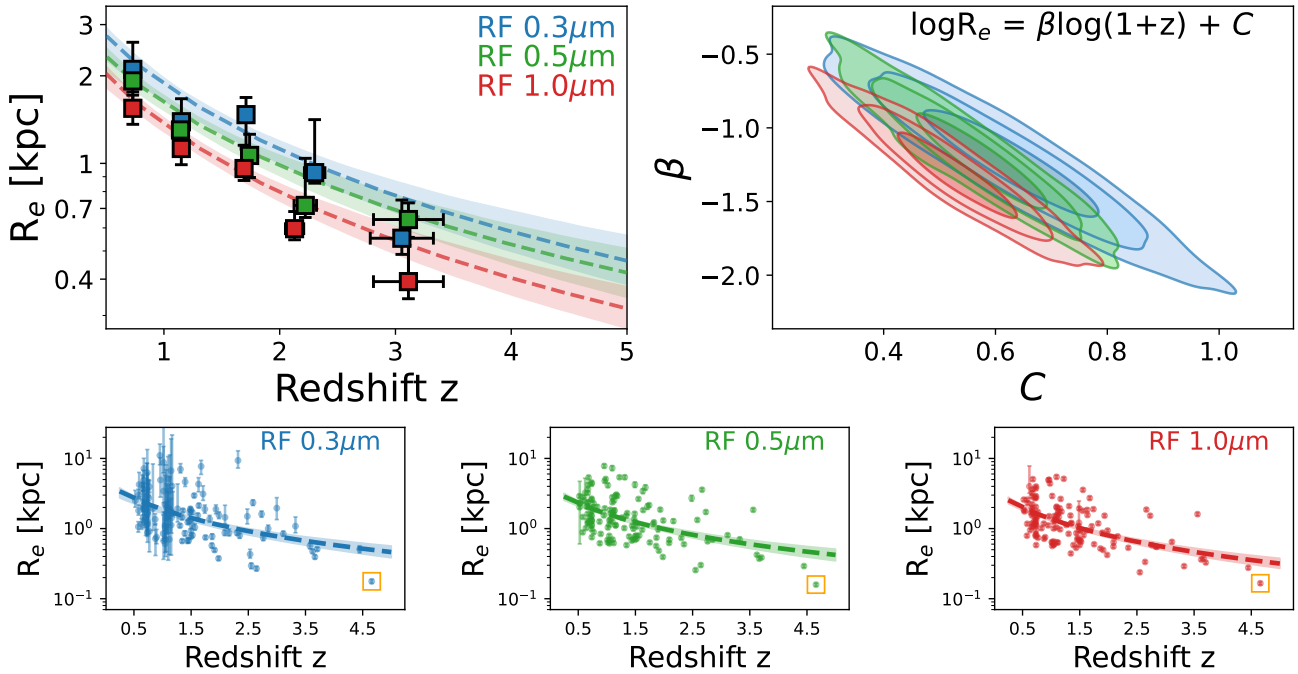

Figure 8. Rest-frame size evolution of massive quiescent galaxies. The corresponding best-fit parameters can be found in Table 1. Top panels: the top-left panel shows the best-fit size evolution at rest-frame 0.3 μm (blue), 0.5 μm (green), and 1 μm (red), respectively. The shaded regions mark the 1σ uncertainties of the best-fit relations. The filled squares with error bars are median R_e and their uncertainties in individual redshift bins (Section 5.2). The top-right panel shows the 1σ, 2σ, and 3σ contours of the R_e–z relations based on our bootstrap Monte Carlo method (Section 5.2). Bottom panels: differing from the top-left panel, here we plot individual quiescent galaxies to the size-evolution diagram. Like previous figures, GS-9209 is marked with the orange square.

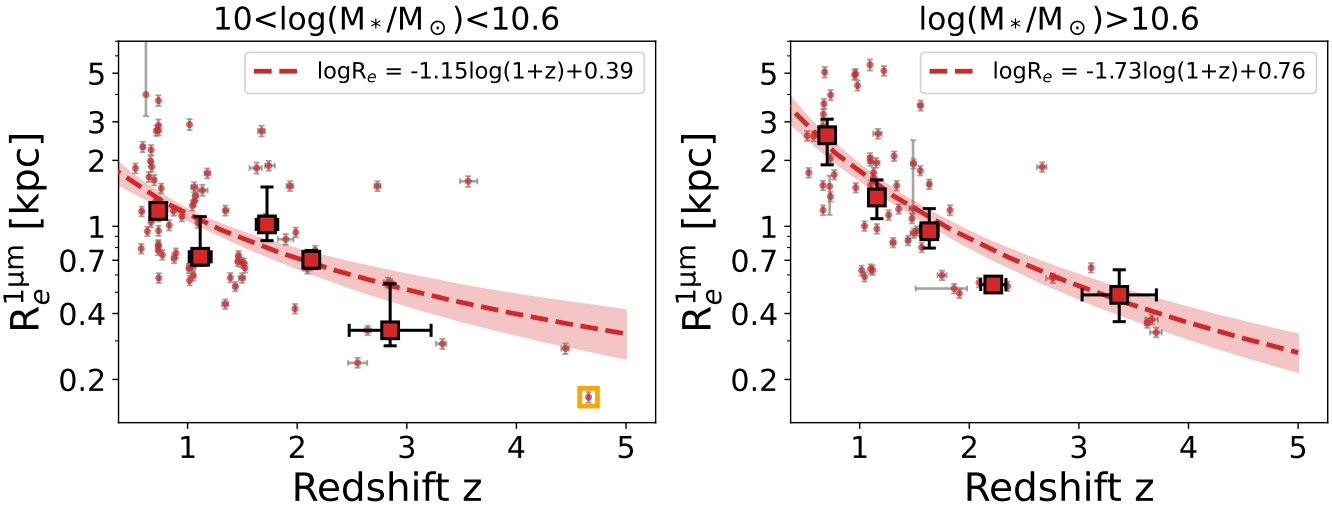

Figure 9. Stellar-mass dependence of the size evolution at rest-1 μm. The left panel shows the size evolution of quiescent galaxies with $\log(M_*/M_\odot) = 10 - 10.6$, while the right panel shows the evolution for those with $\log(M_*/M_\odot) > 10.6$. Little dots are individual quiescent galaxies, and large squares are the median size of each redshift bin (the same as Figure 8). The dashed red line shows the best-fit evolution (Equation (3)), and the shaded region marks the 1σ uncertainty estimated using the bootstrap Monte Carlo method. The size evolution is faster for more-massive quiescent galaxies. A similar trend is also found for the size evolution at rest-0.3 and 0.5 μm (Table 2). Like previous figures, GS-9209 is marked with the orange square.

Table 2
Stellar-mass Dependence of the Size Evolution of Massive Quiescent Galaxies (Equation (3))

$\lambda_{\rm rest}$	$M_* = 10^{10} \sim 10^{10.6}\,M_\odot$		$M_* > 10^{10.6}\,M_\odot$	
	β	C	β	C
0.3 μm	$-1.06^{+0.31}_{-0.33}$	$0.50^{+0.12}_{-0.12}$	$-1.68^{+0.27}_{-0.28}$	$0.87^{+0.14}_{-0.14}$
0.5 μm	$-1.04^{+0.25}_{-0.26}$	$0.43^{+0.08}_{-0.09}$	$-1.60^{+0.29}_{-0.22}$	$0.79^{+0.09}_{-0.11}$
1 μm	$-1.15^{+0.25}_{-0.22}$	$0.38^{+0.08}_{-0.07}$	$-1.73^{+0.24}_{-0.20}$	$0.76^{+0.09}_{-0.09}$

We attempt to constrain the key physical quantity driving the differences in morphology at different rest wavelengths. In Figure 11, we plot the rest-NIR to optical size ratio, i.e., $R_e^{1\,\mu\rm m}/R_e^{0.5\,\mu\rm m}$, as a function of the mass-weighted stellar age. Because the strength of color gradients depends on stellar mass (C. Tortora et al. 2010; K. A. Suess et al. 2019b; A. van der Wel et al. 2023), we separate our sample into two stellar-mass bins using $\langle \log(M_*/M_\odot)\rangle = 10.6$, the median value of the entire sample. Regardless of stellar mass, younger quiescent galaxies with ages $\leqslant$1.5 Gyr

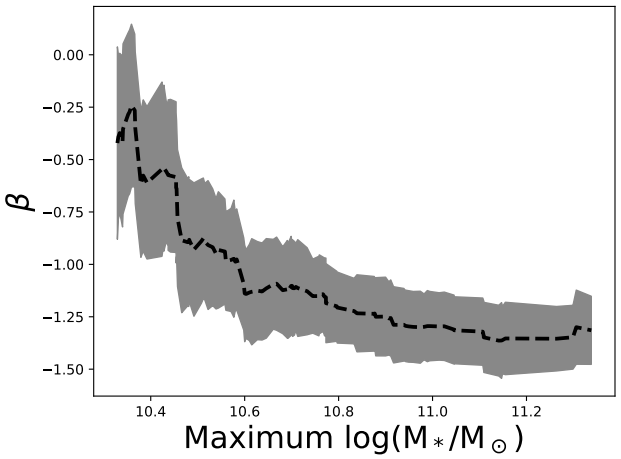

Figure 10. The change of the best-fit β (Equation (3)) as more massive quiescent galaxies are included in the fit (black solid line). The x-axis shows the maximum stellar mass of the quiescent galaxies included in the fit (see Section 5.2.1 for details). The gray shaded regions mark the 1σ uncertainty estimated using the bootstrap Monte Carlo method. As more massive quiescent galaxies are added to the fit, the slope β becomes more negative, i.e., the size evolution is faster for more-massive quiescent galaxies.

have relatively flat color gradients, i.e., $R_e^{1\,\mu m}/R_e^{0.5\,\mu m}$ closer to 1, in broad agreement with studies of post-starburst galaxies (D. T. Maltby et al. 2018; K. A. Suess et al. 2020). As galaxies become older (>1.5 Gyr), we observe an increase in the number of quiescent galaxies with large difference in rest-optical and NIR morphologies ($R_e^{1\,\mu m}/R_e^{0.5\,\mu m} < 0.8$). Color gradients of older quiescent galaxies are more negative, i.e., their centers are redder. This is consistent with the general picture of inside-out growth of massive galaxies, followed by inside-out quenching, where galaxies built up their centers earlier than outskirts (e.g., S. Tacchella et al. 2015; E. J. Nelson et al. 2016; Z. Ji & M. Giavalisco 2023).

We see tentative evidence that old (>1.5 Gyr), higher-mass quiescent galaxies have flatter color gradients than lower-mass ones. The median size ratio $\langle R_e^{1\,\mu m}/R_e^{0.5\,\mu m}\rangle$ is 0.87 ± 0.02 for $\log(M_*/M_\odot) > 10.6$ quiescent galaxies, whereas it is 0.83 ± 0.02 for $10 < \log(M_*/M_\odot) < 10.6$ ones (the quoted uncertainty is estimated following the bootstrap Monte Carlo method). This is in line with the studies of nearby massive ($\log(M_*/M_\odot) > 10$) galaxies from SDSS: C. Tortora et al. (2010) found that the most-massive ($\log(M_*/M_\odot) > 11$) early-type galaxies have almost flat color gradients, which become increasingly more negative as early-type galaxies become less massive. This finding needs to be tested with future larger samples of massive quiescent galaxies at high redshifts.

We also check the relationship of $R_e^{1\,\mu m}/R_e^{0.5\,\mu m}$ with dust attenuation $E(B-V)$ and stellar metallicity Z_*. We do not see clear trends, although this may be a result of the degeneracy between $E(B-V)$ and Z_* that makes the inference of them individually highly uncertain with photometric data only. We defer detailed analysis of the spatially resolved stellar populations of the quiescent galaxies to a future study aimed at dissecting the physical mechanism(s) behind this finding.

Finally, in addition to $R_e^{1\,\mu m}/R_e^{0.5\,\mu m}$, we have also studied the trends discussed above using $R_e^{1\,\mu m}/R_e^{0.3\,\mu m}$. We do not find any substantial changes in our conclusions, although the measurement of $R_e^{1\,\mu m}/R_e^{0.3\,\mu m}$ is noisier than $R_e^{1\,\mu m}/R_e^{0.5\,\mu m}$ as quiescent galaxies are fainter in rest-UV than in rest-optical.

5.2.3. Comparing the Size Evolution of This Work with Other Studies

We first compare our results with HST studies. A. van der Wel et al. (2014) combined all five CANDELS fields to measure the rest-0.5 μm size evolution over $0 < z < 2.5$. Our new measurements obtain $\beta \approx -1.25 \pm 0.20$ (Table 1), which is broadly consistent with A. van der Wel et al. (2014), who found $-1.3 \lesssim \beta \lesssim -1$ for $\log(M_*/M_\odot) > 10$ quiescent galaxies (see their Table 2). This shows that the size evolution of quiescent galaxies established based on rest-optical HST imaging still holds with the deeper, higher-resolution JWST/NIRCam observations.

More specifically, regarding the size evolution of quiescent galaxies with $\log(M_*/M_\odot) = 10 - 10.6$, we obtain $\beta = -1.04^{+0.25}_{-0.26}$ (Table 2), which is in quantitative agreement with A. van der Wel et al. (2014), who found $\beta = -1.01 \pm 0.06$ for quiescent galaxies of similar stellar masses. Regarding the higher-mass ones, i.e., $\log(M_*/M_\odot) > 10.6$, we obtain $\beta = -1.60^{+0.29}_{-0.22}$, compared to $\beta = -1.32 \pm 0.21$ from A. van der Wel et al. (2014). Statistically, this difference in β is marginal, $\lesssim 1\sigma$. Nonetheless, we still investigate what causes the marginally steeper size evolution we found for the $\log(M_*/M_\odot) > 10.6$ quiescent galaxies. First, this is not due to the systematics in the size measures between JWST and HST, as we found consistent sizes between the measurements using NIRCam/F150W and HST/F160W imaging (Section 4.2). Second, we note that with HST, A. van der Wel et al. (2014) was only able to measure the rest-optical size evolution up to $z = 2.5$, whereas with JADES, we can now extend the size measurements of quiescent galaxies beyond $z > 2.5$. If we only include $z < 2.5$ galaxies in the fit, we will still find a similarly steeper size evolution than A. van der Wel et al. (2014). Therefore, the steeper size evolution from our measurements is not due to including $z > 2.5$ quiescent galaxies either. The main cause for the steeper size evolution seems to be sample selection. The analysis of A. van der Wel et al. (2014) included all *UVJ* quiescent galaxies selected based on 3D-HST rest-frame colors, while we removed from our analysis 36 out of 197 galaxies that do not satisfy the *UVJ* criteria any more after we re-fit their SEDs with new photometry from JADES (Section 3). If those 36 galaxies were not removed, we would have found $\beta = -1.30 \pm 0.27$, which is fully consistent with A. van der Wel et al. (2014). We note that the majority—22 out of 36—of the removed galaxies are at $z > 1.5$, most of which are near the *UVJ* selection boundaries. Interestingly, the removed galaxies generally have more extended morphologies than those retained in our final sample, indicating a strong correlation between the size and star formation properties of galaxies at Cosmic Noon (R. J. Williams et al. 2010; S. Wuyts et al. 2011; S. G. Patel et al. 2013; A. van der Wel et al. 2014; Z. Ji & M. Giavalisco 2023, to name a few).

We now compare our results with a very recent JWST study done by A. van der Wel et al. (2023), who measured the size evolution of massive quiescent galaxies using NIRCam data from the CEERS survey. A. van der Wel et al. (2023) obtained $\beta = -1.70 \pm 0.10$ for $\log(M_*/M_\odot) > 11$, $0.5 < z < 2.3$ quiescent galaxies. If we fit the size evolution only for a subsample of the same redshift and stellar-mass ranges, we will obtain a fully consistent $\beta \approx -1.75$. Moreover, A. van der Wel et al. (2023) found that the pace of the size evolution does not depend on size proxies used (e.g., half-light versus half-mass). This is also similar to our finding above that β does not

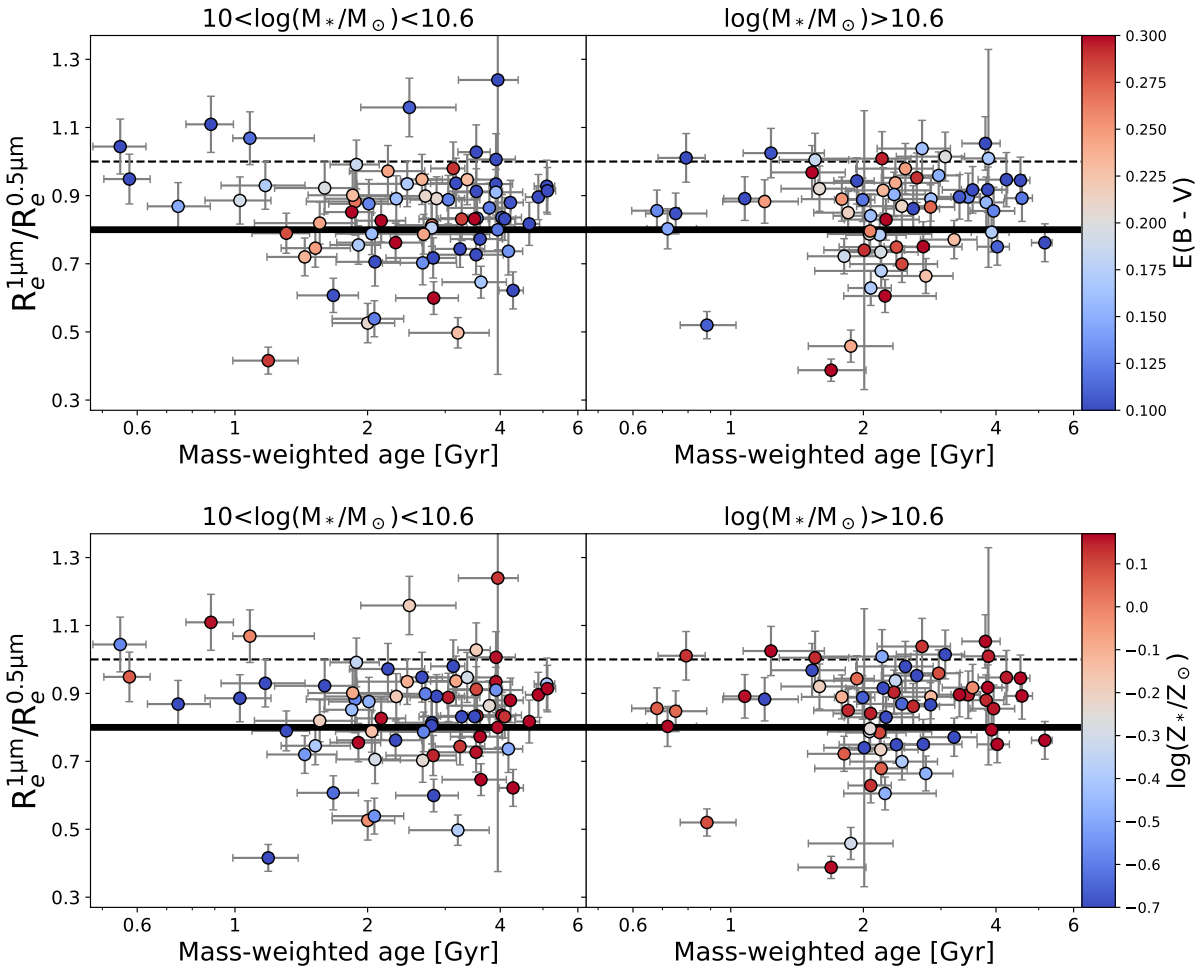

Figure 11. The ratio of rest-1 μm size to rest-0.5 μm size as a function of mass-weighted stellar age. In the top panel, galaxies are color-coded according to the color excess $E(B-V)$, while in the bottom panel, galaxies are color-coded according to the stellar metallicity Z_*. The horizontal dashed line marks $R_e^{1\,\mu m}/R_e^{0.5\,\mu m}=1$, i.e., no evidence of color gradients. The black solid line marks $R_e^{1\,\mu m}/R_e^{0.5\,\mu m}=0.8$, about the median value of all quiescent galaxies in this study. Younger quiescent galaxies in general have rest-optical to rest-NIR size ratios closer to unity, i.e., an indication of flatter color gradients. As they become older, we observe an emergence of quiescent galaxies with large color gradients, i.e., $R_e^{1\,\mu m}/R_e^{0.5\,\mu m}<0.8$.

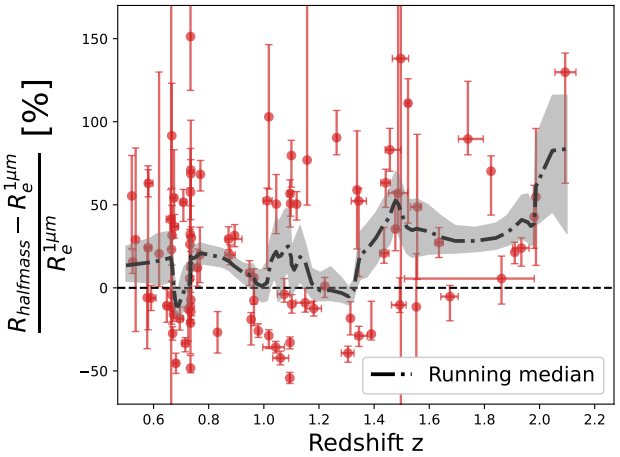

Figure 12. Relative difference between $R_e^{1\mu m}$ and the half-mass sizes from K. A. Suess et al. (2019b) as a function of redshift. The gray dashed–dotted line and shaded region show the running median and its 1σ uncertainty, respectively. The uncertainty of the relative difference (y-axis) is dominated by the uncertainty of half-mass–size measurements from K. A. Suess et al. (2019b).

depend on rest-frame wavelengths where the sizes are measured (Table 1 and Figure 8).

Our results—and hence those of A. van der Wel et al. (2023)—then suggest significant size evolution of massive quiescent galaxies beyond $z>1$, which is in tension with some previous studies based on HST imaging: K. A. Suess et al. (2020) and T. B. Miller et al. (2023) found that the half-mass–size evolution of quiescent galaxies is slower than their rest-optical, half-light size evolution, suggesting that the latter is mostly due to stellar mass-to-light radio gradients, rather than the intrinsic growth of galaxies' sizes. In Figure 12, for the subsample having $R_{\rm halfmass}$ from K. A. Suess et al. (2020), we plot the relative difference between $R_{\rm halfmass}$ and $R_e^{1\mu m}$ as a function of redshift. We also plot the running median and its uncertainty estimated following the bootstrap Monte Carlo method described earlier (Section 5.2). Up to $z\sim1.2$, the median of the relative difference remains roughly flat, with $R_{\rm halfmass}$ being larger than $R_e^{1\mu m}$ by $14\%\pm8\%$. Although the sample size of quiescent galaxies having both $R_{\rm halfmass}$ and $R_e^{1\mu m}$ measurements is limiting at $z>1.2$, we see evidence that $R_{\rm halfmass}$ becomes increasingly larger than $R_e^{1\mu m}$ toward higher

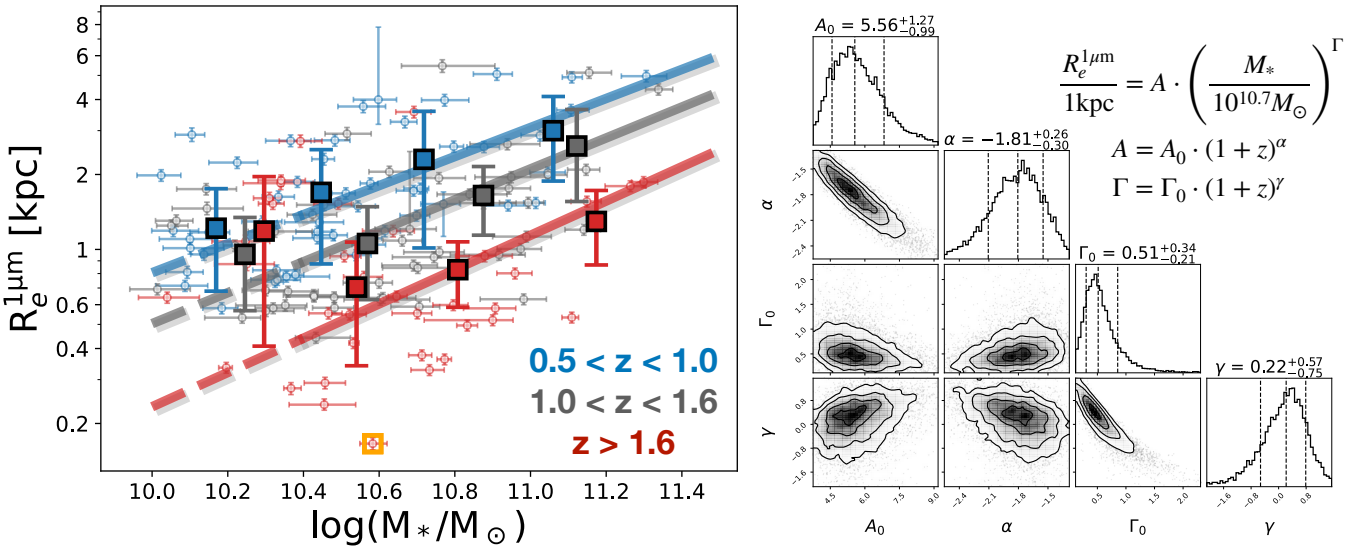

Figure 13. Stellar mass–size relationship of massive quiescent galaxies. In the left panel, we show the scatter plot of stellar masses vs. rest-1 μm sizes, where the entire sample is divided into three groups using redshift terciles. Small dots show the individual measurements, and large squares show the median sizes of individual stellar-mass bins. For galaxies with $\log(M_*/M_\odot) \geqslant 10.4$, we fit the redshift-dependent mass–size relationship using the functional form shown on the right (see Section 5.3 for details). Solid lines show the best-fit relationships at the median redshifts of the three groups. We also extrapolate the relation to $\log(M_*/M_\odot) < 10.4$, shown as dashed lines. The right panel shows the corner plots for the fitted parameters of the mass–size relationship. Like before, GS-9209 is marked with the orange square.

redshifts. This explains the shallower half-mass–size evolution at $z > 1$ reported by those earlier HST studies. A. van der Wel et al. (2023; see their Appendix A) also attempted to address this tension regarding the half-mass–size evolution at $z > 1$ by comparing the light-to-mass weighed size ratios from their measurements with those from K. A. Suess et al. (2020). Similar to what we found in Figure 12, A. van der Wel et al. (2023) showed that, while the light-to-mass weighed size ratio from K. A. Suess et al. (2020) becomes increasingly larger at $z > 1.5$, they did not see this trend in their new measurements using CEERS data.

We point out that the methods used to derive the half-mass sizes are dramatically different in the literature, which can lead to inconsistent conclusions about the size evolution of quiescent galaxies. For example, also using HST imaging, M. Mosleh et al. (2017) adopted a different approach to account for the radial gradient of the stellar mass-to-light ratio. Unlike K. A. Suess et al. (2020) and T. B. Miller et al. (2023), M. Mosleh et al. (2017) found that half-mass sizes of quiescent galaxies significantly evolve at $z > 1$. In the future, dedicated analysis of different methodologies in deriving the half-mass sizes, and larger samples of quiescent galaxies at $z > 2$ are needed to finally address this tension between JWST and HST studies.

5.3. Stellar Mass–Size Relationship of Massive Quiescent Galaxies

We now present the mass–size relationship of massive quiescent galaxies. To characterize it, we assume the functional form of

$$R_e^{1\mu m}\,[\text{kpc}] = A \cdot \left(\frac{M_*}{10^{10.7} M_\odot}\right)^{\Gamma}, \quad (4)$$

where both the amplitude A and power-law index Γ depend on redshifts following $A = A_0(1+z)^{\alpha}$ and $\Gamma = \Gamma_0(1+z)^{\gamma}$. It has been shown by previous studies that the mass–size relationship of quiescent galaxies cannot be well described by a single power law, where the relationship becomes flattened below the pivot mass $\sim 10^{10.4} M_\odot$ (e.g., A. van der Wel et al. 2014, 2023; S. E. Cutler et al. 2022). Therefore, we only fit Equation (4) for galaxies with $M_* > 10^{10.4} M_\odot$. Like before, we estimate the uncertainties of the fitted parameters using the bootstrap Monte Carlo method: We bootstrap the entire sample, use normal distributions to Monte Carlo resample the M_* and $R_e^{1\mu m}$ measures using their corresponding uncertainties, and finally fit the mass–size relationship. We repeat this procedure 10,000 times and use the range between the 16th and 84th percentiles as 1σ uncertainties.

In Figure 13 we show the mass–size relationship. The amplitude A strongly evolves with redshift following $(1+z)^{-1.8}$, showing that at a fixed stellar mass, quiescent galaxies are significantly larger at lower redshifts. The slope of the mass–size relationship is $\Gamma_0 \sim 0.5$, and it does not strongly depend on redshift with γ being consistent with 0, in broad agreement with previous studies (A. van der Wel et al. 2014; L. Mowla et al. 2019). We note, however, that the current sample size of $z > 3$ quiescent galaxies is very limiting, and future larger samples are needed to check if the slope of the mass–size relationship persists toward higher redshifts. Finally, for completeness, we also report the best-fit mass–size relationships of the rest-frame 0.3 and 0.5 μm sizes in Table 3.

Table 3
The Best-fit Mass–Size Relationship of Massive Quiescent Galaxies (Equation (4))

$\lambda_{\rm rest}$	A_0 (kpc)	α	Γ_0	γ
0.3 μm	$8.43^{+2.10}_{-1.58}$	$-1.78^{+0.26}_{-0.30}$	$0.49^{+0.49}_{-0.28}$	$0.17^{+0.78}_{-0.94}$
0.5 μm	$5.04^{+1.02}_{-0.73}$	$-1.41^{+0.22}_{-0.26}$	$0.48^{+0.31}_{-0.20}$	$0.33^{+0.63}_{-0.71}$
1 μm	$5.56^{+1.27}_{-0.99}$	$-1.81^{+0.26}_{-0.30}$	$0.51^{+0.34}_{-0.21}$	$0.22^{+0.57}_{-0.75}$

6. Discussion

With the deep, multiband JWST/NIRCam imaging data from JADES, we have studied the size evolution of a robust sample of massive quiescent galaxies with $\log(M_*/M_\odot) > 10$ over $0.5 < z < 5$. Regardless of the rest-frame wavelengths where the sizes are measured, we observed strong size evolution of massive quiescent galaxies. This evolution depends on stellar mass, with more-massive quiescent galaxies having faster evolution in size. In the following, we will discuss in detail the implications of the observed size evolution on the formation and evolution of quiescent galaxies across cosmic time. We will also discuss our findings with regard to the quiescent galaxies at $z > 3$.

6.1. Physical Mechanisms Driving the Size Evolution of Quiescent Galaxies

Two broad categories of physical mechanisms can drive the strong size evolution of quiescent galaxies without significantly increasing their stellar masses. First, in ΛCDM cosmology, at a fixed mass, galaxies that formed later are expected to be larger, known as the progenitor effect (C. M. Carollo et al. 2013; S. J. Lilly & C. M. Carollo 2016; Z. Ji & M. Giavalisco 2022). It is therefore possible that the apparent size evolution of quiescent galaxies is driven by the addition of newly quenched, larger galaxies at lower redshifts. Alternatively, post-quenching growth—particularly mechanisms such as gas-poor minor mergers that can efficiently grow sizes without significantly increasing masses—can also explain the observed strong size evolution (e.g., R. Bezanson et al. 2009; T. Naab et al. 2009).

Regarding the progenitor effect, there is a simple prediction for the pace of apparent size evolution. Specifically, by construction, the virial radius ($R_{\rm vir}$) of a dark matter halo is set by the threshold of density contrast—the ratio of density to the mean density of the Universe—at the redshift of halo collapse ($z^{\rm h}_{\rm form}$). Because the density contrast threshold has a very weak time dependence, we then expect that, at a fixed halo mass, $R_{\rm vir}$ should linearly scale with the size of the Universe, i.e., $R_{\rm vir} \propto H(z^{\rm h}_{\rm form})^{-2/3}$ where $H(z^{\rm h}_{\rm form})$ is the Hubble constant at $z^{\rm h}_{\rm form}$ (H. Mo et al. 2010). Given that $H(z) \sim (1+z)^{1.4}$ at Cosmic Noon $z \sim 2$, we would then expect $R_{\rm V\,ir} \propto (1+z^{\rm h}_{\rm form})^{-1}$. Finally, because the ratio of the galaxy R_e to the halo $R_{\rm V\ ir}$ is roughly constant, as supported by both theories (e.g., H. Mo et al. 2010) and observations (e.g., A. V. Kravtsov 2013; R. S. Somerville et al. 2018), the prediction for the apparent size evolution driven by the progenitor effect is then $R_e \propto (1+z^{\rm h}_{\rm form})^{-1}$.

6.1.1. Lower-mass Quiescent Galaxies with $10 < \log(M_*/M_\odot) < 10.6$

The size evolution of $10^{10}M_\odot < M_* < 10^{10.6}M_\odot$ quiescent galaxies follows $(1+z)^{-1.15^{+0.25}_{-0.22}}$ (Section 5.2), which is broadly consistent with $R_e \propto (1+z)^{-1}$ and hence is in line with the progenitor effect.

Before moving forward, we clarify several things with regard to the comparison between the observed size evolution and the prediction of the progenitor effect. First, the prediction is made for galaxies at a fixed halo mass, rather than a fixed stellar mass. However, we note that the stellar-mass range considered here—$10^{10}M_\odot < M_* < 10^{10.6}M_\odot$—is where galaxies' halo masses do not change substantially over $0.5 < z < 5$ (see, e.g., the left panel of Figure 7 in P. S. Behroozi et al. 2013a). If we use the relationship between stellar mass and halo mass from P. S. Behroozi et al. (2013a, 2013b),[32] we find that the halo masses of our quiescent samples at different redshifts are very similar, with the median halo mass being $10^{12}M_\odot$ for the $z > 2$ subsample compared to $10^{11.9}M_\odot$ for the $z < 2$ subsample.

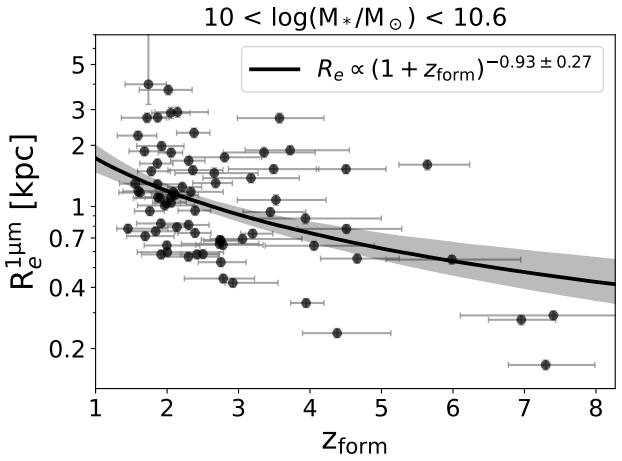

Figure 14. $R_e^{1\mu m}$ as a function of formation redshift ($z_{\rm form}$) for quiescent galaxies with $10 < \log(M_*/M_\odot) < 10.6$. The relationship between $R_e^{1\mu m}$ and $z_{\rm form}$ is broadly consistent with $(1+z_{\rm form})^{-1}$, in line with the expectation from the progenitor effect (Section 6.1.1).

Second, the halo formation theory detailed above, if applicable, suggests that the size of galaxies should more tightly correlate with $z^{\rm h}_{\rm form}$, the time of halo formation, than with z, the time of observation. Following Z. Ji & M. Giavalisco (2022), instead of using z, we study the relationship between R_e and the formation redshift, $z_{\rm form}$, which is defined as the redshift when a galaxy reached its mass-weighted age. As Figure 14 shows, the best-fit relationship is $R_e^{1\mu m} \propto (1+z_{\rm form})^{-0.93\pm0.27}$. Compared to $\beta = -1.15$ obtained for the relationship between $R_e^{1\mu m}$ and z (Section 5.2), using $z_{\rm form}$ makes the slope of the size evolution closer to -1, i.e., the prediction of the progenitor effect. We note, however, that using $z_{\rm form}$ as a proxy for $z^{\rm h}_{\rm form}$ is purely from an empirical standpoint, and very likely there are better metrics, which is, however, beyond the scope of this work.

Finally, in addition to fitting the size evolution as a function of $(1+z)$, which is widely used in the literature but arguably not the best physically motivated form in terms of halo formation (see description above and also A. van der Wel et al. 2014), we also fit the size evolution as a function of the Hubble constant $H(z)$, i.e., $R_e \propto H(z)^{\beta_H}$. We find $\beta_H = -0.87^{+0.21}_{-0.15}$ for the relationship between $R_e^{1\mu m}$ and $H(z)$, and $\beta_H = -0.64^{+0.23}_{-0.17}$ for the relationship between $R_e^{1\mu m}$ and $H(z_{\rm form})$. Similarly, the best-fit β_H of the relationship between $R_e^{1\mu m}$ and $z_{\rm form}$ is closer to $\beta_H = -2/3$ predicted by the progenitor effect.

Obviously, the interpretation of the observed slope of size evolution is highly degenerated, as the slope might reflect either a single, dominated physical mechanism or the interplay among several mechanisms that can mimic a similar size evolution. Nonetheless, particularly because the slope becomes

[32] At $z \leqslant 5$, the data release of P. S. Behroozi et al. (2013a, 2013b) only contains six redshift slices, i.e., $z = 0.1, 1, 2, 3, 4, 5$. We therefore interpolate those slices to derive the halo mass of a galaxy at its exact redshift value.

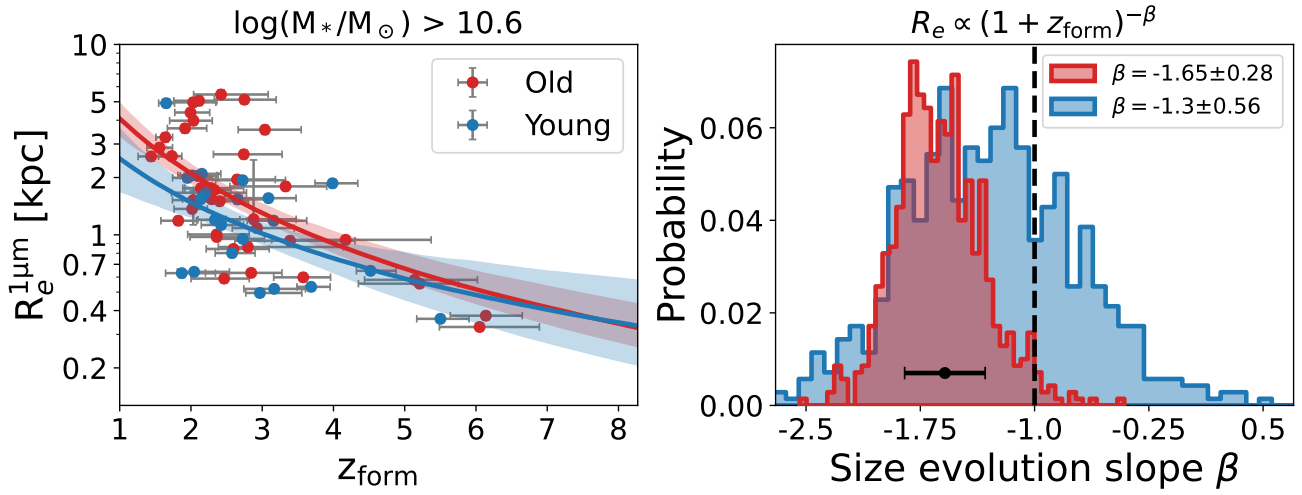

Figure 15. $R_e^{1\mu m}$ as a function of formation redshift (z_{form}) for quiescent galaxies with $\log(M_*/M_\odot) > 10.6$. We divide the sample into old (red) and young (blue) subsamples (Section 6.1.2). The left panel shows the best-fit relationship between $R_e^{1\mu m}$ and z_{form}. The right panel shows the distributions of β for the two subsamples from our bootstrap Monte Carlo method (Section 6.1.2). The black circle with error bars shows the median and standard deviation of β derived for the entire $\log(M_*/M_\odot) > 10.6$ sample. The vertical, black dashed line marks $\beta = -1$, the expectation from the progenitor effect. Old quiescent galaxies have a steeper $R_e^{1\mu m}$–z_{form} relationship, while the relationship of young quiescent galaxies is closer to $\beta = -1$, i.e., the progenitor effect.

closer to the predicted value of the progenitor effect after switching from z to z_{form}, we believe that the progenitor effect may be the primary mechanism, if not the only one, driving the apparent size evolution observed in the quiescent galaxies with $10 < \log(M_*/M_\odot) < 10.6$. If this indeed is not a coincidence, our findings will then indicate that the size of quiescent galaxies evolves at a similar pace following their dark matter halos. Because of this, we speculate that dark matter halos play a key role, if not the only one, in the quenching and structural evolution of galaxies of this stellar-mass range, which has been suggested by some theoretical works (e.g., Y. Birnboim & A. Dekel 2003; A. Cattaneo et al. 2006; A. Dekel & Y. Birnboim 2006; Z. Chen et al. 2020).

6.1.2. *Higher-mass Quiescent Galaxies with* $\log(M_*/M_\odot) > 10.6$

Relative to the lower-mass ones, the size of higher-mass quiescent galaxies increases faster with cosmic time (Section 5.2.1). The higher-mass quiescent galaxies also have a steeper relationship between $R_e^{1\mu m}$ and z_{form} with a slope of -1.57 ± 0.26. These deviate from the prediction of the progenitor effect alone, suggesting additional mechanism(s) contributing to the structural growth.

Higher-mass quiescent galaxies are hosted by more-massive halos formed in larger overdensities (H. Mo et al. 2010). Consequently, they are expected to experience more merger events than lower-mass galaxies (e.g., P. F. Hopkins et al. 2010a; Y.-j. Peng et al. 2010; V. Rodriguez-Gomez et al. 2015; J. A. O'Leary et al. 2021). Therefore, a likely explanation for their apparent steeper size evolution is the increasing contribution of post-quenching size growth from mergers, especially minor mergers that can grow galaxies' sizes more efficiently than major mergers for a fixed amount of mass to be added to the central galaxy (e.g., R. Bezanson et al. 2009; T. Naab et al. 2009).

If post-quenching mergers do play a significant role in growing the size of higher-mass quiescent galaxies, one would then expect that the slope of the relationship between $R_e^{1\mu m}$ and z_{form} depends on galaxy ages, as older galaxies have more time to alter their structure through mergers. Motivated by this, we divide the higher-mass quiescent sample into the young and old subsamples. Because galaxies at high redshifts are generally younger, instead of making the division using the median age of the entire sample, we first estimate the running median of stellar ages as a function of redshift. The old (young) subsample contains galaxies older (younger) than the median stellar age of their redshifts.

We study the relationship between $R_e^{1\mu m}$ and z_{form} for the young and old subsamples, respectively. To estimate uncertainties of the fitted parameters, we use the bootstrap Monte Carlo method that has been described previously (e.g., Sections 5.2 and 5.3). As Figure 15 shows, although the current sample size is still limiting, we see evidence that the relationship between $R_e^{1\mu m}$ and z_{form} depends on stellar ages. The old subsample has a steeper (more negative) slope than the young subsample. Interestingly, although the slope (-1.30 ± 0.56) observed in the young quiescent subsample is still somewhat steeper, it is broadly consistent with -1 within uncertainty, and is closer to the expectation from the progenitor effect than the old subsample. This finding is consistent with the picture that, apart from the progenitor effect, mergers and/or post-quenching continuous gas accretion drive additional, apparent size growth in very massive quiescent galaxies. As they become older, massive quiescent galaxies experience more merger events that can effectively grow their sizes by adding mass to outskirts.

The conclusions above based on size evolution are in line with other analysis of quiescent galaxies at Cosmic Noon. First, our conclusions are consistent with the stacking analysis of quiescent galaxies' surface brightness profiles at $z \sim 2$ (see Z. Ji & M. Giavalisco 2022) and at $z \sim 0$ (S. Huang et al. 2013a, 2013b), and also in broad agreement with other earlier studies, both observationally and theoretically, where they concluded the mass and size growths of massive quiescent galaxies have a significant contribution from minor mergers at $z < 2$ (e.g., R. Bezanson et al. 2009; P. G. van Dokkum et al. 2010; L. Oser et al. 2012; V. Rodriguez-Gomez et al. 2016). Our conclusions are further supported by a recent JWST study by K. A. Suess et al. (2023), who reported the detection of a large population of low-mass companions within 35 kpc of

quiescent galaxies with $\log(M_*/M_\odot) > 10.5$ at $0.5 < z < 3$. Our conclusions are also in line with recent Atacama Large Millimeter/submillimeter Array observations for a small number of massive quiescent galaxies at $z \sim 0.7$, where the larger-size extended ones simultaneously show evidence for minor merging both in their SFHs and newly accreted gas (J. Spilker et al. 2018; C. Woodrum et al. 2022).

While so far we lack the kinematics constraints for our high-redshift quiescent galaxies, it is worth pointing out that the observed stellar-mass dependence of the size evolution is consistent with the dynamical studies of early-type galaxies (ETGs) at lower redshifts. At intermediate redshifts, R. Bezanson et al. (2018) showed that ETGs at $z \sim 0.8$ become increasingly velocity dispersion dominated as they become more massive. In addition, by studying the excess kurtosis h_4 of the stellar velocity distribution in $z < 1$ quiescent galaxies, F. D'Eugenio et al. (2023) showed that h_4—a sensitive probe of the radial anisotropy of the stellar velocity distribution—increases with cosmic time. At $z \sim 0$, M. Cappellari (2016, and references therein) showed that the distribution of the dynamical state of ETGs is bimodal—fast and slow rotators characterized by very different ratios of rotational velocity to velocity dispersion. The two populations can be very well separated using the stellar mass, with the slow rotators being more massive than the faster rotators (see a recent review by M. Cappellari 2016). All of these dynamical studies suggest that very massive galaxies after quenching continue growing their sizes via merging with other galaxies through dynamical friction. Because multiple incoherent merging events are expected to cause the loss of angular momentum (e.g., E. Emsellem et al. 2011), very massive galaxies eventually become velocity dispersion dominated, i.e., slower rotators .

6.2. The Structure of Quiescent Galaxies at z > 3

The deep JWST/NIRCam imaging from JADES enables us to select robust samples of quiescent galaxies, and to measure their rest-optical and NIR morphologies with high precision beyond $z > 3$. Despite that the current sample size is very limiting, our results suggest that the $z > 3$ quiescent galaxies in our sample have very small sizes, potentially being even smaller than extrapolating the size evolution of lower-redshift quiescent galaxies (Section 5.2). A similar finding is reported by L. Wright et al. (2023), who found evidence that $z > 3$ massive quiescent galaxies in CEERS also seem to be more compact than previously anticipated. In what follows, we take a close look at the structural properties of the $z > 3$ quiescent galaxies in this study.

6.2.1. Large Stellar Mass Surface Densities of the Freshly Quenched z > 3 Galaxies

Among 11 photometrically robust quiescent galaxies at $z > 3$ in our sample, eight have reliable R_e estimates from single-Sérsic fitting (Section 4.2). We calculate their stellar mass surface densities within the half-light radius following $\Sigma_e = M_*/(2\pi R_e^2)$.

The remaining three galaxies have best-fit $n = 8$, and they have very compact cores, as PSF spikes are clearly seen in their F444W images. While the galaxies with $n = 8$ were removed from all analysis presented above, here we attempt to give reasonable Σ_e estimates for these three galaxies as well. Instead of using R_e from single-Sérsic fitting, we thus use the sizes of the three galaxies from the Richardson–Lucy deconvolution approach (Section 4.2.1).

We compare the Σ_e of the $z > 3$ quiescent galaxies with galaxies at $1 < z < 3$ from CANDELS. For CANDELS galaxies, we make use of the stellar-mass measures from B. Lee et al. (2018) and rest-optical sizes measured with HST/WFC3 imaging. For consistency, we thus use rest-0.5 μm sizes to calculate Σ_e for the $z > 3$ galaxies, although we have already checked that any of our conclusions will not change if we use rest-1 μm sizes instead. As Figure 16 shows, the vast majority of the $z > 3$ quiescent galaxies are very compact, with $\Sigma_e > 10^{10}\,M_\odot\,\mathrm{kpc}^{-2}$. Such a stellar mass surface density is comparable to that observed in nuclear star clusters in nearby galaxies (M. A. Norris et al. 2014), and it is also above the averaged value found in quiescent galaxies at lower redshifts and significantly exceeds that observed in star-forming galaxies of similar stellar masses at Cosmic Noon (e.g., G. Barro et al. 2017; Z. Ji & M. Giavalisco 2023).

We note that the presence of AGNs can make galaxies appear smaller than they actually are, because the nonstellar, nucleated light from AGNs can lead to a smaller size from single-Sérsic fitting than the intrinsic one of stellar distribution (Z. Ji et al. 2022). Despite that AGN-hosting galaxies have already been removed from our sample through various AGN selection methods (Section 3), there could still be some missed ones, because the AGNs are too faint to be identified by those selection methods. One example is GS-9209—it shows a broad Hα emission line but is not identified as an AGN based on SED fitting—which we will discuss in detail in Section 6.2.2. Although we currently do not know how many of the $z > 3$ quiescent galaxies in our sample might host a similarly faint broad-line AGN like GS-9209, we argue this does not seem to be able to explain the strong size evolution, hence the very large Σ_e of the $z > 3$ quiescent galaxies for the following two main reasons. First, the SED shapes of the quiescent galaxies all seem to be typical for quiescent/post-starburst galaxies, with no clear evidence of hosting strong AGNs of known types. Second, the broad emission lines from AGNs, if present, likely can only affect the rest-0.5 μm sizes (due to, e.g., [O III] 5007 Å), while they should have much less of an effect on the rest-1 μm sizes, because this wavelength range is mostly free of strong emission lines. Yet, we still observe the very strong size evolution at rest-frame 1 μm. Moreover, even for AGNs hosting galaxies (e.g., X-ray or IRAC-selected AGNs), their rest-optical light is still predominantly from stars. The impact of AGNs, if not accounted for during morphological fitting, can only affect the size measurement on the order of $\approx$10% (see Figure 7 in Z. Ji et al. 2022), which is insufficient to explain the very large Σ_e obtained here. Therefore, we argue that the very large Σ_e found here are most likely due to the very compact stellar-mass distributions in the $z > 3$ quiescent galaxies.

The strong correlation between the mass surface density and star formation properties found at low redshifts has long been suggested as an indication of the causal link between the buildup of central regions of galaxies and quenching (G. Kauffmann et al. 2003; M. Franx et al. 2008; E. Cheung et al. 2012; G. Barro et al. 2017; B. Lee et al. 2018; Z. Ji & M. Giavalisco 2023, just to name a few). However, because the most quiescent galaxies observed at $z < 3$ are already old, with a typical stellar age of > 1 Gyr (A. C. Carnall et al. 2019; Z. Ji & M. Giavalisco 2022; S. Tacchella et al. 2022), such a

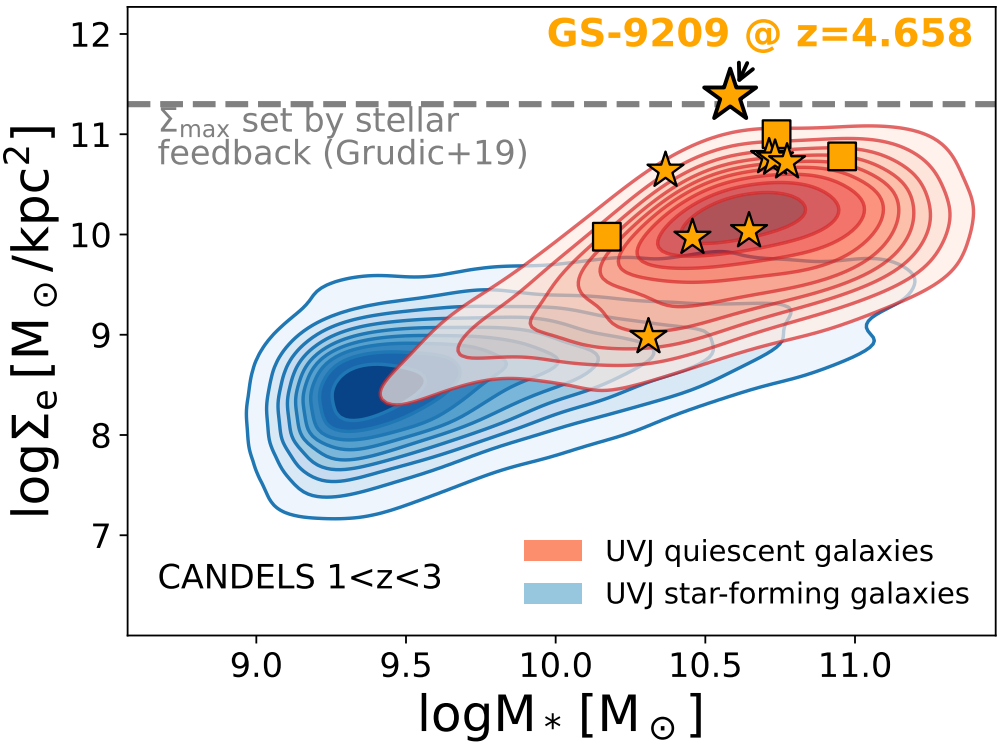

Figure 16. Stellar mass surface density within effective radius (Σ_e) vs. M_*. Background contours show density distributions of *UVJ*-selected star-forming (blue) and quiescent (red) galaxies at $1 < z < 3$ from CANDELS. There are 11 robust quiescent galaxies at $z > 3$ in our sample, among which eight (shown as orange stars) have reliable size estimates from single-Sérsic fitting, including the galaxy GS-9209 that is highlighted with an enlarged symbol. For the remaining three galaxies (shown as orange squares), we calculate their Σ_e using alternative size measures (see Section 6.2.1 for details). The gray horizontal dashed line marks the maximum value of stellar mass surface density theoretically derived by M. Y. Grudić et al. (2019).

timescale is comparable to/longer than some post-quenching processes required to alter galaxy structures (e.g., see Figure 10 in L. J. Tacconi et al. 2020). This makes it difficult to definitively answer whether the large mass surface densities found in quiescent galaxies are the cause or the consequence of quenching, or a byproduct of an as-yet-unidentified physical process. Compared to the lower-redshift ones, the $z > 3$ quiescent galaxies presented here are much younger, with stellar ages ranging from 100–700 Myr and with a typical value of 500 Myr. These freshly quenched galaxies are already compact, suggesting the possible coeval formation of dense central regions and quenching at $z > 3$, which is consistent with a recent JWST study of $3 < z < 4.5$ galaxies with forming stellar cores (Z. Ji et al. 2023).

6.2.2. GS-9209 at $z_{spec} = 4.658$

The most remarkable $z > 3$ quiescent galaxy in our sample is GS-9209, one of the earliest massive quiescent galaxy known so far having spectroscopically confirmed $z_{\rm spec} = 4.658$ with JWST/NIRSpec observations (A. C. Carnall et al. 2023b). The NIRSpec spectrum of GS-9209 is very similar to typical post-starburst galaxies, showing prominent stellar absorption features of A-type stars. Despite that an AGN is not needed to fit GS-9209's broadband SED, a broad Hα emission line with FWHM $\sim 10^4$ km s^{-1} is observed in the NIRSpec spectrum, indicating that the galaxy actually hosts a faint AGN (A. C. Carnall et al. 2023b). Moreover, as Figure 16 shows, the galaxy has an extreme Σ_e, namely that it is comparable to the maximum allowed stellar mass surface density set by stellar feedback (M. Y. Grudić et al. 2019).

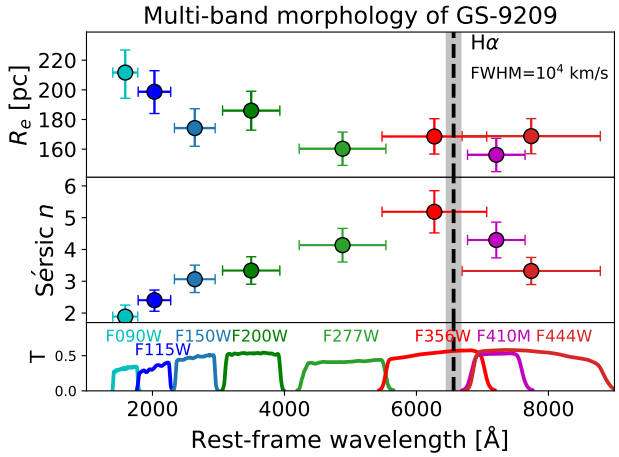

Figure 17. Multiband morphologies of GS-9209 in NIRCam images from JADES. The black, vertical dashed line marks Hα emission, and the shaded gray region corresponds to FWHM =10, 000 km s^{-1} measured by A. C. Carnall et al. (2023b). Generally speaking, from rest-UV to NIR, GS-9209 becomes more compact (smaller R_e) and spheroidal (larger Sérsic n). Evidence of broad Hα affecting the light distribution in F356W is also observed.

With deep NIRCam images from JADES, we measure the multiband morphologies for GS-9209. The results are shown in Figure 17. A. C. Carnall et al. (2023b) reported a size of 215 ± 20 pc using the NIRCam F210M (rest-0.4 μm) image from JEMS (C. C. Williams et al. 2023), which is consistent with our measurement, where we obtain the half-light semimajor radius of 223 ± 16 pc (or 186 ± 13 pc for circularized size R_e) in F200W. As the top panel of Figure 17 shows, overall, the size of GS-9209 decreases

with wavelength—its light distribution becomes more compact at longer wavelength. The R_e of the galaxy is 160 ± 11 pc in F277W (rest-0.5 μm) and 168 ± 12 pc in F444W (rest-1 μm), which are $2 \sim 3$ times smaller than the sizes predicted by using our best-fit size evolution (Section 5.2). In addition, shown in the middle panel of Figure 17 that the Sérsic index n also changes with wavelength. The morphology of GS-9209 gets more spheroidal at longer wavelengths. The best-fit Sérsic index is $n = 1.8 \pm 0.4$ in F090W (rest-1500 Å), whereas it becomes $n = 3.3 \pm 0.4$ in F444W (rest-1 μm). These immediately show the presence of radial color gradient in GS-9209. The galaxy is more extended in rest-UV and optical than in rest-NIR, either due to the radial gradient of dust attenuation, where the central regions of the galaxy either have more dust, or older stellar populations, or both.

Finally, we also note the sudden change of the light distribution of GS-9209 in F356W where the Hα emission of the galaxy is covered. The galaxy is more nucleated (Sérsic $n = 5.2 \pm 0.7$) in F356W than in adjacent filters, as the AGN Hα emission comes from the very central parts of the galaxy. In the future, we may be able to recover some faint high-redshift AGN candidates missed by photometric selection methods through morphological analysis of deep NIRCam images, once the galaxies' redshifts are well constrained.

7. Caveats

We summarize here the main caveats of this work, particularly those associated with our conclusions regarding quiescent galaxies at $z > 3$.

Our quiescent-galaxy sample is drawn from the JADES imaging in GOODS-South, which (at the time of this analysis) covers only $\sim$60 arcmin^2. Consequently, while the data are ultra-deep, the number ($\sim$10) of massive quiescent galaxies at $z > 3$ remains small. This limited sample size prevents us from drawing statistically significant conclusions about the size evolution of quiescent galaxies at $z > 3$. However, since there is currently a lack of systematic environmental analyses for $z > 3$ quiescent galaxies, and there is no indication that the $z > 3$ quiescent galaxies in GOODS-S reside in large-scale structures (e.g., overdensities) that differ significantly from the underlying quiescent population at these redshifts, it is reasonable to regard the $z > 3$ objects in our sample as a randomly drawn, small subsample of the underlying quiescent population. We therefore consider them to provide meaningful, if limited, insights into the structural properties of quiescent galaxies at these early epochs.

We remind the reader that our size-evolution fits are performed on individual galaxies (Section 5.2), and the sample is dominated by lower-redshift objects (most lie at $z \lesssim 2$), which therefore drive the best-fit size-evolution parameters. We report the empirical observation that the $z > 3$ quiescent galaxies in our sample appear very compact and may lie below an extrapolation of the lower-redshift size–redshift relation. However, we stress that we do *not* claim that the current dataset can statistically establish whether the slope of size evolution changes at $z > 3$; doing so will require substantially larger $z > 3$ quiescent samples from wider-area JWST imaging.

Similarly, we emphasize that the best-fit size–mass relation obtained in Section 5.3 should be used with caution at $z > 3$ given the very limited sample size.

At $z > 3$, many quiescent galaxies are very compact and approach the regime where the PSF, the degeneracy between R_e and Sérsic index n, and potential mismatches between real light profiles and single-Sérsic models can impact parametric size measurements. To assess the robustness of our conclusions, we compared our fiducial GALFIT sizes to multiple alternative approaches (Lenstronomy, fixed-n fits, and a nonparametric Richardson–Lucy deconvolution-based estimate), finding that the different methods correlate well and that the relative size differences are typically $\lesssim$50% for the majority of the $z > 3$ objects. Nevertheless, for the most extreme systems, GALFIT can converge to the imposed upper bound in n (and/or yield very compact cores), in which case parametric size estimates become less reliable. We treat such cases conservatively in our analysis and rely on alternative size estimates where appropriate. Future studies that characterize the detailed light distributions of $z > 3$ quiescent-galaxy populations (e.g., using multicomponent modeling and nonparametric structural diagnostics), together with realistic image simulations that forward-model compact galaxies through the PSF, noise, and fitting pipelines, will be essential to quantify and correct systematic uncertainties in size measurements for these extremely compact systems.

8. Summary

In this work, we studied the size evolution of massive quiescent galaxies with $\log(M_*/M_\odot) > 10$ at $0.5 < z < 5$. With multiband deep NIRCam imaging from the JADES survey in the GOODS-South field, we characterized the size evolution of massive quiescent galaxies from UV–NIR at three different wavelengths, namely rest-frame 0.3, 0.5, and 1 μm. We found the following:

1. Regardless of wavelengths, the size of massive quiescent galaxies strongly evolves with cosmic time following $R_e \propto (1+z)^{-1.3}$. The pace of size evolution depends on stellar mass, with the evolution being faster for more-massive galaxies. Specifically, the size evolution follows $R_e \propto (1+z)^{-1.1}$ for lower-mass quiescent galaxies with $10 < \log(M_*/M_\odot) < 10.6$, while it follows $R_e \propto (1+z)^{-1.7}$ for higher-mass quiescent galaxies with $\log(M_*/M_\odot) > 10.6$ (Section 5.2.1).
2. As a result of negative stellar mass-to-light ratio, the size of quiescent galaxies decreases with wavelength. Relative to their rest-1 μm sizes, on average, quiescent galaxies are larger by 45% at rest-0.3 μm and 15% at rest-0.5 μm, showing that the stellar mass distribution of quiescent galaxies is more compact than the rest-UV and optical light distributions. Evidence that younger quiescent galaxies have shallower color gradients than older ones is also seen, but requires future larger quiescent samples to test (Section 5.2.2).
3. At a fixed stellar mass, the size of quiescent galaxies is significantly larger at lower redshifts. The slope of the relationship between stellar mass and size only very weakly, if at all, depends on redshift; although, we stress that the current sample size of $z > 3$ quiescent galaxies is very limiting and future larger samples are needed to check if the slope remains unchanged toward higher redshifts (Section 5.3).

We discussed possible physical mechanisms responsible for the observed size evolution. In particular, we studied the

relationship between R_e and $z_{\rm form}$, the formation redshift of galaxies. We showed the following:

1. For lower-mass ($10 < \log(M_*/M_\odot) < 10.6$) quiescent galaxies, the slope of the relationship between R_e and $z_{\rm form}$ is consistent with -1, the prediction of the progenitor effect. Thus, we think that the progenitor effect may play a significant role in driving the apparent size evolution of quiescent galaxies of this stellar-mass range (Section 6.1.1).
2. For higher-mass ($\log(M_*/M_\odot) > 10.6$) quiescent galaxies, the relationship between R_e and $z_{\rm form}$ depends on stellar age. For young quiescent galaxies, the slope of the R_e–$z_{\rm form}$ relationship is consistent with -1 within uncertainty (though somewhat steeper), whereas for old quiescent galaxies, the relationship is much steeper than the prediction of the progenitor effect alone. These are in line with the picture that, in addition to the progenitor effect, mergers and/or post-quenching continuous gas accretion drive additional, apparent size growth in very massive quiescent galaxies (Section 6.1.2).

Notwithstanding the very limited sample size, we studied the structure of massive quiescent galaxies at $z > 3$ in this work. We saw evidence that these quiescent galaxies are even smaller than anticipated using the best-fit size evolution derived for lower-redshift quiescent galaxies (Section 5.2.1). Moreover, we showed that these freshly quenched quiescent galaxies, with a typical stellar age of 500 Myr compared to >1 Gyr observed in quiescent galaxies at lower redshifts, are already very compact, with $\Sigma_e \gtrsim 10^{10} M_\odot\,{\rm kpc}^{-2}$, suggesting the possible coeval formation of dense central regions and quenching at $z > 3$ (Section 6.2). We also studied in detail the multiband morphology for GS-9209 (A. C. Carnall et al. 2023b), one of the earliest massive quiescent galaxies known so far with $z_{\rm spec} = 4.658$. From rest-UV to NIR, we found that GS-9209 becomes increasingly smaller and more compact, and its light profile becomes more spheroidal, showing that the radial color gradient is already present in this earliest massive quiescent galaxy (Section 6.2.2).

Finally, as a closing remark, we note that the current high-redshift quiescent sample, e.g., at $z > 3$, is still small. Explicitly and better constraining the size evolution at $z > 3$ will await larger samples selected from JWST imaging, and this motivates future analysis based on robustly JWST-selected high-redshift samples (e.g., S. Alberts et al. 2023) over larger sky areas. We also stress that characterizing the size evolution really is just the first step to constrain the formation pathways of the first quiescent galaxies in the Universe. The structure of the earliest quiescent galaxies is likely much more complex. Some hints have already been seen from our Figure 5: sizes from the Richardson–Lucy deconvolution approach are larger than those from the single-Sérsic fitting. This suggests multicomponent structures are already present in quiescent galaxies at $z > 3$. With the superb NIR imaging from JWST, we will be able to study such complex structural properties in the earliest quiescent galaxies in unprecedented detail.

Acknowledgments

Z.J., B.D.J., B.E.R., Z.C., C.D., D.J.E., E.E., K.H., J.M.H., G.R., M.R., F.S., and C.N.A.W. acknowledge support from JWST/NIRCam contract to the University of Arizona, NAS5-02015. The research of C.C.W. is supported by NOIRLab, which is managed by the Association of Universities for Research in Astronomy (AURA) under a cooperative agreement with the National Science Foundation. B.E.R. acknowledges support from JWST Program 3215. S.A. acknowledges support from the JWST Mid-Infrared Instrument (MIRI) Science Team Lead, grant 80NSSC18K0555, from NASA Goddard Space Flight Center to the University of Arizona. W.B., F.D.E., T.J.L., R.M., L.S., and J.W. acknowledge support by the Science and Technology Facilities Council (STFC), by the ERC through Advanced Grant 695671 "QUENCH." K.B. acknowledges support in part by the Australian Research Council Centre of Excellence for All Sky Astrophysics in 3 Dimensions (ASTRO 3D), through project No. CE170100013. A.J.B. and J.C. acknowledge funding from the "FirstGalaxies" Advanced Grant from the European Research Council (ERC) under the European Union's Horizon 2020 research and innovation program (grant agreement No. 789056). S.C. acknowledges support by European Union's HE ERC Starting grant No. 101040227—WINGS. E.C.L. acknowledges support of an STFC Webb Fellowship (ST/W001438/1). D.J.E. is supported as a Simons Investigator. R.H. acknowledges that funding for this research was provided by the Johns Hopkins University, Institute for Data Intensive Engineering and Science (IDIES). R.M. acknowledges support by the UKRI Frontier Research grant RISEandFALL, and funding from a research professorship from the Royal Society. H.Ü. gratefully acknowledges support by the Isaac Newton Trust and by the Kavli Foundation through a Newton–Kavli Junior Fellowship. H.Ü. acknowledges funding by the European Union (ERC APEX, 101164796). Views and opinions expressed are, however, those of the authors only and do not necessarily reflect those of the European Union or the European Research Council Executive Agency. Neither the European Union nor the granting authority can be held responsible for them.

This work made use of the *lux* supercomputer at UC Santa Cruz, which is funded by NSF MRI grant AST 1828315, as well as the High Performance Computing (HPC) resources at the University of Arizona, which is funded by the Office of Research Discovery and Innovation (ORDI), Chief Information Officer (CIO), and University Information Technology Services (UITS).

Facilities: HST (ACS, WFC3), JWST (NIRCam).

Software: GALFIT (C. Y. Peng et al. 2010), PROSPECTOR (B. D. Johnson et al. 2021), FSPS (C. Conroy et al. 2009; C. Conroy & J. E. Gunn 2010), MIST (J. Choi et al. 2016; A. Dotter 2016), MILES (J. Falcón-Barroso et al. 2011), ASTROPY (Astropy Collaboration et al. 2022), PHOTUTILS (L. Bradley et al. 2023), WEBBPSF (M. D. Perrin et al. 2014), NUMPY (C. R. Harris et al. 2020), SCIPY (P. Virtanen et al. 2020), CORNER (D. Foreman-Mackey 2016).

Appendix
SED Fitting with Different SFHs

We test our SED fitting with different assumptions of SFHs. Specifically, in Figure 18, we compare the physical quantities derived using our fiducial SED assumptions, i.e., nonparametric SFHs with the Dirichlet prior (Section 4.1), with those derived using nonparametric SFHs with the continuity prior. These two nonparametric SFH priors are very similar, except that the continuity prior disfavors sudden changes of SFRs in adjacent lookback time bins (see J. Leja et al. 2019 for details).

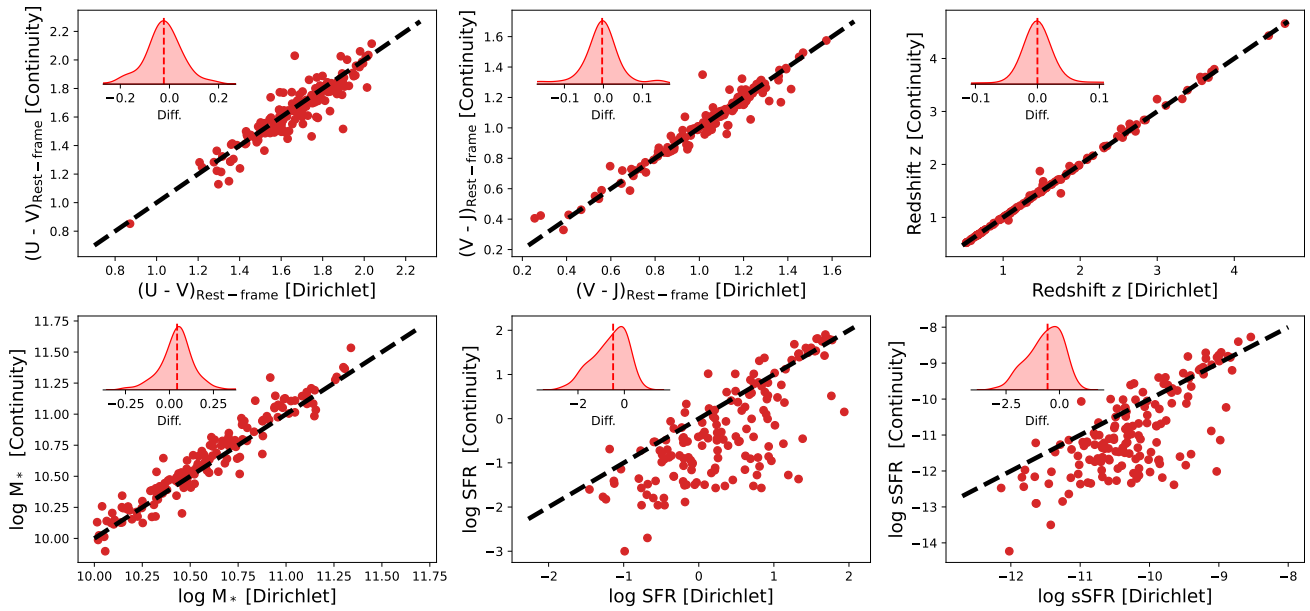

Figure 18. Comparison of physical properties derived from nonparametric SFHs with the Dirichlet prior (x-axis) and nonparametric SFHs with the continuity prior (y-axis).

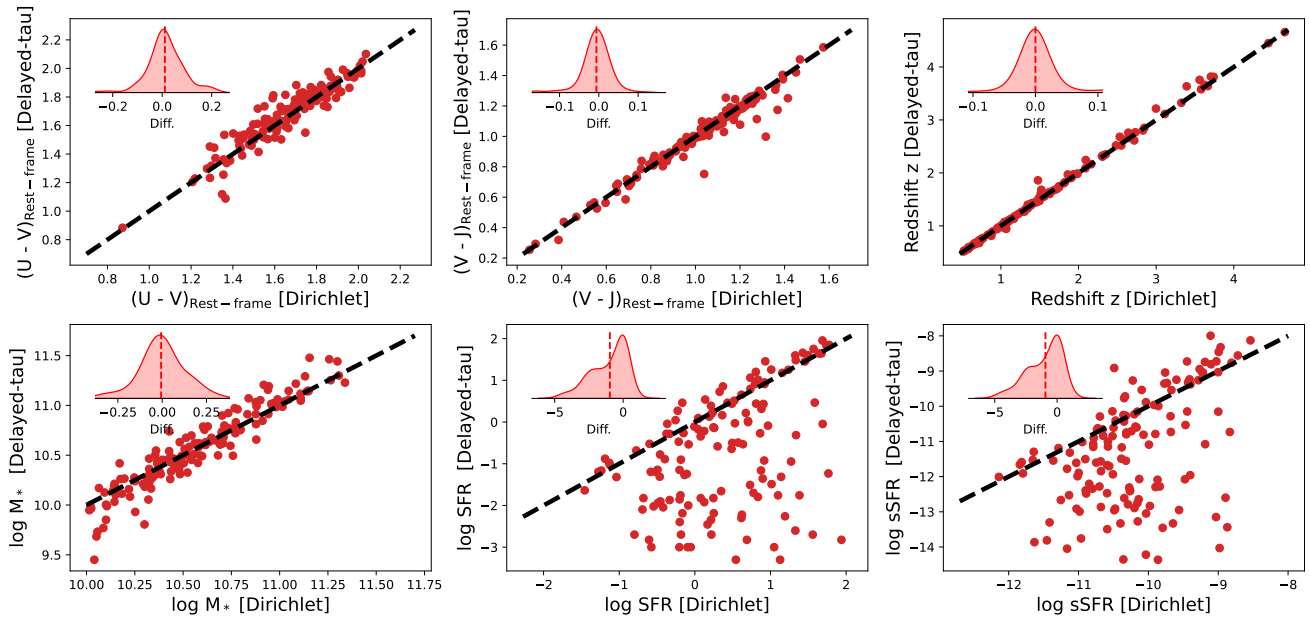

Figure 19. Similar to Figure 18, but now we compare the physical properties from nonparametric Dirichlet SFHs with those from parametric delayed-tau SFHs.

Similarly, in Figure 19, we compare our fiducial SED-fitting results with those derived using parametric delayed-tau SFHs. Stellar masses, redshifts, and rest-frame *UVJ* colors agree very well among different SFH assumptions. Systematic offsets exist for the SFR measures for quiescent galaxies, as expected for SED fitting with photometric data only (C. Conroy 2013).

ORCID iDs

Zhiyuan Ji https://orcid.org/0000-0001-7673-2257
Christina C. Williams https://orcid.org/0000-0003-2919-7495
Katherine A. Suess https://orcid.org/0000-0002-1714-1905
Sandro Tacchella https://orcid.org/0000-0002-8224-4505
Benjamin D. Johnson https://orcid.org/0000-0002-9280-7594
Brant Robertson https://orcid.org/0000-0002-4271-0364
Stacey Alberts https://orcid.org/0000-0002-8909-8782
William M. Baker https://orcid.org/0000-0003-0215-1104
Stefi Baum https://orcid.org/0000-0002-4735-8224
Rachana Bhatawdekar https://orcid.org/0000-0003-0883-2226
Nina Bonaventura https://orcid.org/0000-0001-8470-7094
Kristan Boyett https://orcid.org/0000-0003-4109-304X
Andrew J. Bunker https://orcid.org/0000-0002-8651-9879
Stefano Carniani https://orcid.org/0000-0002-6719-380X
Stephane Charlot https://orcid.org/0000-0003-3458-2275
Zuyi Chen https://orcid.org/0000-0002-2178-5471
Jacopo Chevallard https://orcid.org/0000-0002-7636-0534
Emma Curtis-Lake https://orcid.org/0000-0002-9551-0534

Francesco D'Eugenio https://orcid.org/0000-0003-2388-8172
Anna de Graaff https://orcid.org/0000-0002-2380-9801
Christa DeCoursey https://orcid.org/0000-0002-4781-9078
Eiichi Egami https://orcid.org/0000-0003-1344-9475
Daniel J. Eisenstein https://orcid.org/0000-0002-2929-3121
Kevin Hainline https://orcid.org/0000-0003-4565-8239
Ryan Hausen https://orcid.org/0000-0002-8543-761X
Jakob M. Helton https://orcid.org/0000-0003-4337-6211
Tobias J. Looser https://orcid.org/0000-0002-3642-2446
Jianwei Lyu https://orcid.org/0000-0002-6221-1829
Roberto Maiolino https://orcid.org/0000-0002-4985-3819
Michael V. Maseda https://orcid.org/0000-0003-0695-4414
Erica Nelson https://orcid.org/0000-0002-7524-374X
George Rieke https://orcid.org/0000-0003-2303-6519
Marcia Rieke https://orcid.org/0000-0002-7893-6170
Hans-Walter Rix https://orcid.org/0000-0003-4996-9069
Lester Sandles https://orcid.org/0000-0001-9276-7062
Fengwu Sun https://orcid.org/0000-0002-4622-6617
Hannah Übler https://orcid.org/0000-0003-4891-0794
Christopher N. A. Willmer https://orcid.org/0000-0001-9262-9997
Chris Willott https://orcid.org/0000-0002-4201-7367
Joris Witstok https://orcid.org/0000-0002-7595-121X

References

Alberts, S., Williams, C. C., Helton, J. M., et al. 2024, ApJ, 975, 85
Anderson, J., & King, I. R. 2000, PASP, 112, 1360
Astropy Collaboration, Price-Whelan, A. M., Lim, P. L., et al. 2022, ApJ, 935, 167
Baker, W. M., Lim, S., D'Eugenio, F., et al. 2025a, MNRAS, 539, 557
Baker, W. M., Valentino, F., Lagos, C. d. P., et al. 2025b, A&A, 702, A270
Barro, G., Faber, S. M., Koo, D. C., et al. 2017, ApJ, 840, 47
Behroozi, P. S., Wechsler, R. H., & Conroy, C. 2013a, ApJ, 770, 57
Behroozi, P. S., Wechsler, R. H., & Conroy, C. 2013b, ApJL, 762, L31
Bell, E. F., & de Jong, R. S. 2001, ApJ, 550, 212
Belli, S., Newman, A. B., & Ellis, R. S. 2019, ApJ, 874, 17
Bezanson, R., van der Wel, A., Pacifici, C., et al. 2018, ApJ, 858, 60
Bezanson, R., van Dokkum, P. G., Tal, T., et al. 2009, ApJ, 697, 1290
Birnboim, Y., & Dekel, A. 2003, MNRAS, 345, 349
Bradley, L., Sipőcz, B., Robitaille, T., et al. 2023, Astropy/photutils: v1.8.0, Zenodo, doi: 10.5281/zenodo.7946442
Brammer, G. B., van Dokkum, P. G., Franx, M., et al. 2012, ApJS, 200, 13
Byler, N., Dalcanton, J. J., Conroy, C., & Johnson, B. D. 2017, ApJ, 840, 44
Cappellari, M. 2016, ARA&A, 54, 597
Carnall, A. C., McLure, R. J., Dunlop, J. S., et al. 2019, MNRAS, 490, 417
Carnall, A. C., Walker, S., McLure, R. J., et al. 2020, MNRAS, 496, 695
Carnall, A. C., McLeod, D. J., McLure, R. J., et al. 2023a, MNRAS, 520, 3974
Carnall, A. C., McLure, R. J., Dunlop, J. S., et al. 2023b, Natur, 619, 716
Carollo, C. M., Bschorr, T. J., Renzini, A., et al. 2013, ApJ, 773, 112
Cassata, P., Giavalisco, M., Williams, C. C., et al. 2013, ApJ, 775, 106
Cattaneo, A., Dekel, A., Devriendt, J., Guiderdoni, B., & Blaizot, J. 2006, MNRAS, 370, 1651
Charlot, S., & Fall, S. M. 2000, ApJ, 539, 718
Chen, Z., Faber, S. M., Koo, D. C., et al. 2020, ApJ, 897, 102
Cheung, E., Faber, S. M., Koo, D. C., et al. 2012, ApJ, 760, 131
Choi, J., Dotter, A., Conroy, C., et al. 2016, ApJ, 823, 102
Conroy, C. 2013, ARA&A, 51, 393
Conroy, C., & Gunn, J. E. 2010, ApJ, 712, 833
Conroy, C., Gunn, J. E., & White, M. 2009, ApJ, 699, 486
Cutler, S. E., Whitaker, K. E., Mowla, L. A., et al. 2022, ApJ, 925, 34
Daddi, E., Renzini, A., Pirzkal, N., et al. 2005, ApJ, 626, 680
Damjanov, I., Abraham, R. G., Glazebrook, K., et al. 2011, ApJL, 739, L44
Davari, R., Ho, L. C., Peng, C. Y., & Huang, S. 2014, ApJ, 787, 69
Dekel, A., & Birnboim, Y. 2006, MNRAS, 368, 2
D'Eugenio, F., van der Wel, A., Piotrowska, J. M., et al. 2023, MNRAS, 525, 2789
Donley, J. L., Koekemoer, A. M., Brusa, M., et al. 2012, ApJ, 748, 142
Donnari, M., Pillepich, A., Nelson, D., et al. 2019, MNRAS, 485, 4817
Dotter, A. 2016, ApJS, 222, 8
Eisenstein, D. J., Willott, C., Alberts, S., et al. 2023, arXiv:2306.02465
Emsellem, E., Cappellari, M., Krajnović, D., et al. 2011, MNRAS, 414, 888
Falcón-Barroso, J., Sánchez-Blázquez, P., Vazdekis, A., et al. 2011, A&A, 532, A95
Fan, L., Lapi, A., Bressan, A., et al. 2010, ApJ, 718, 1460
Foreman-Mackey, D. 2016, JOSS, 1, 24
Franx, M., van Dokkum, P. G., Förster Schreiber, N. M., et al. 2008, ApJ, 688, 770
Gaia Collaboration, Brown, A. G. A., Vallenari, A., et al. 2021, A&A, 649, A1
Gardner, J. P., Mather, J. C., Abbott, R., et al. 2023, PASP, 135, 068001
Giavalisco, M., Ferguson, H. C., Koekemoer, A. M., et al. 2004, ApJL, 600, L93
Glazebrook, K., Nanayakkara, T., Schreiber, C., et al. 2024, Natur, 628, 277
Grudić, M. Y., Hopkins, P. F., Quataert, E., & Murray, N. 2019, MNRAS, 483, 5548
Guo, Y., Ferguson, H. C., Giavalisco, M., et al. 2013, ApJS, 207, 24
Harris, C. R., Millman, K. J., van der Walt, S. J., et al. 2020, Natur, 585, 357
Hopkins, P. F., Bundy, K., Murray, N., et al. 2009, MNRAS, 398, 898
Hopkins, P. F., Bundy, K., Croton, D., et al. 2010a, ApJ, 715, 202
Hopkins, P. F., Murray, N., Quataert, E., & Thompson, T. A. 2010b, MNRAS, 401, L19
Huang, S., Ho, L. C., Peng, C. Y., Li, Z.-Y., & Barth, A. J. 2013a, ApJ, 766, 47
Huang, S., Ho, L. C., Peng, C. Y., Li, Z.-Y., & Barth, A. J. 2013b, ApJL, 768, L28
Ilbert, O., McCracken, H. J., Le Fèvre, O., et al. 2013, A&A, 556, A55
Illingworth, G., Magee, D., Bouwens, R., et al. 2016, arXiv:1606.00841
Ji, Z., & Giavalisco, M. 2022, ApJ, 935, 120
Ji, Z., & Giavalisco, M. 2023, ApJ, 943, 54
Ji, Z., Giavalisco, M., Kirkpatrick, A., et al. 2022, ApJ, 925, 74
Ji, Z., Giavalisco, M., Vanzella, E., et al. 2020, ApJ, 888, 109
Ji, Z., Giavalisco, M., Williams, C. C., et al. 2018, ApJ, 862, 135
Ji, Z., Williams, C. C., Tacchella, S., et al. 2024, ApJ, 974, 135
Johnson, B. D., Leja, J., Conroy, C., & Speagle, J. S. 2021, ApJS, 254, 22
Kauffmann, G., Heckman, T. M., White, S. D. M., et al. 2003, MNRAS, 341, 54
Kravtsov, A. V. 2013, ApJL, 764, L31
Kubo, M., Tanaka, M., Yabe, K., et al. 2018, ApJ, 867, 1
Labbé, I., Huang, J., Franx, M., et al. 2005, ApJL, 624, L81
Lee, B., Giavalisco, M., Whitaker, K., et al. 2018, ApJ, 853, 131
Leja, J., Carnall, A. C., Johnson, B. D., Conroy, C., & Speagle, J. S. 2019, ApJ, 876, 3
Leja, J., Johnson, B. D., Conroy, C., van Dokkum, P. G., & Byler, N. 2017, ApJ, 837, 170
Leja, J., Speagle, J. S., Johnson, B. D., et al. 2020, ApJ, 893, 111
Leja, J., Speagle, J. S., Ting, Y.-S., et al. 2022, ApJ, 936, 165
Lilly, S. J., & Carollo, C. M. 2016, ApJ, 833, 1
Lower, S., Narayanan, D., Leja, J., et al. 2020, ApJ, 904, 33
Luo, B., Brandt, W. N., Xue, Y. Q., et al. 2017, ApJS, 228, 2
Lustig, P., Strazzullo, V., D'Eugenio, C., et al. 2021, MNRAS, 501, 2659
Lyu, J., Alberts, S., Rieke, G. H., & Rujopakarn, W. 2022, ApJ, 941, 191
Madau, P. 1995, ApJ, 441, 18
Maltby, D. T., Almaini, O., Wild, V., et al. 2018, MNRAS, 480, 381
McGaugh, S. S., & Schombert, J. M. 2014, AJ, 148, 77
Merlin, E., Castellano, M., Santini, P., et al. 2021, A&A, 649, A22
Miller, T. B., van Dokkum, P., & Mowla, L. 2023, ApJ, 945, 155
Miller, T. B., Whitaker, K. E., Nelson, E. J., et al. 2022, ApJL, 941, L37
Mo, H., van den Bosch, F. C., & White, S. 2010, Galaxy Formation and Evolution (Cambridge Univ. Press)
Mosleh, M., Hosseinnejad, S., Hosseini-ShahiSavandi, S. Z., & Tacchella, S. 2020, ApJ, 905, 170
Mosleh, M., Tacchella, S., Renzini, A., et al. 2017, ApJ, 837, 2
Mowla, L., van der Wel, A., van Dokkum, P., & Miller, T. B. 2019, ApJL, 872, L13
Muzzin, A., Marchesini, D., Stefanon, M., et al. 2013, ApJ, 777, 18
Naab, T., Johansson, P. H., & Ostriker, J. P. 2009, ApJL, 699, L178
Nanayakkara, T., Glazebrook, K., Jacobs, C., et al. 2024, NatSR, 14, 3724
Nelson, E. J., van Dokkum, P. G., Förster Schreiber, N. M., et al. 2016, ApJ, 828, 27
Newman, A. B., Ellis, R. S., Bundy, K., & Treu, T. 2012, ApJ, 746, 162
Norris, M. A., Kannappan, S. J., Forbes, D. A., et al. 2014, MNRAS, 443, 1151
O'Leary, J. A., Moster, B. P., Naab, T., & Somerville, R. S. 2021, MNRAS, 501, 3215

Oser, L., Naab, T., Ostriker, J. P., & Johansson, P. H. 2012, ApJ, 744, 63
Pacifici, C., Iyer, K. G., Mobasher, B., et al. 2023, ApJ, 944, 141
Papovich, C., Kawinwanichakij, L., Quadri, R. F., et al. 2018, ApJ, 854, 30
Patel, S. G., van Dokkum, P. G., Franx, M., et al. 2013, ApJ, 766, 15
Peebles, P. J. E. 1993, Principles of Physical Cosmology (Princeton Univ. Press)
Peng, C. Y., Ho, L. C., Impey, C. D., & Rix, H.-W. 2010, AJ, 139, 2097
Peng, Y.-j., Lilly, S. J., Kovač, K., et al. 2010, ApJ, 721, 193
Perrin, M. D., Sivaramakrishnan, A., Lajoie, C.-P., et al. 2014, SPIE, 9143, 91433X
Planck Collaboration, Aghanim, N., Akrami, Y., et al. 2020, A&A, 641, A6
Prato, M., Cavicchioli, R., Zanni, L., Boccacci, P., & Bertero, M. 2012, A&A, 539, A133
Quadri, R., Marchesini, D., van Dokkum, P., et al. 2007, AJ, 134, 1103
Richardson, W. H. 1972, JOSA, 62, 55
Rieke, M. & the JADES Collaboration 2023, ApJS, 269, 16
Robotham, A. S. G., Taranu, D. S., Tobar, R., Moffett, A., & Driver, S. P. 2017, MNRAS, 466, 1513
Rodriguez-Gomez, V., Genel, S., Vogelsberger, M., et al. 2015, MNRAS, 449, 49
Rodriguez-Gomez, V., Pillepich, A., Sales, L. V., et al. 2016, MNRAS, 458, 2371
Schreiber, C., Pannella, M., Elbaz, D., et al. 2015, A&A, 575, A74
Shen, S., Mo, H. J., White, S. D. M., et al. 2003, MNRAS, 343, 978
Simmonds, C., Tacchella, S., Curtis-Lake, W. M. E., et al. 2025, MNRAS, 544, 4551
Skelton, R. E., Whitaker, K. E., Momcheva, I. G., et al. 2014, ApJS, 214, 24
Somerville, R. S., Behroozi, P., Pandya, V., et al. 2018, MNRAS, 473, 2714
Speagle, J. S., Steinhardt, C. L., Capak, P. L., & Silverman, J. D. 2014, ApJS, 214, 15
Spilker, J., Bezanson, R., Barišić, I., et al. 2018, ApJ, 860, 103
Straatman, C. M. S., Labbé, I., Spitler, L. R., et al. 2015, ApJL, 808, L29
Suess, K. A., Bezanson, R., Nelson, E. J., et al. 2022, ApJL, 937, L33
Suess, K. A., Kriek, M., Price, S. H., & Barro, G. 2019a, ApJL, 885, L22
Suess, K. A., Kriek, M., Price, S. H., & Barro, G. 2019b, ApJ, 877, 103
Suess, K. A., Kriek, M., Price, S. H., & Barro, G. 2020, ApJL, 899, L26
Suess, K. A., Williams, C. C., Robertson, B., et al. 2023, ApJL, 956, L42
Tacchella, S., Carollo, C. M., Renzini, A., et al. 2015, Sci, 348, 314
Tacchella, S., Conroy, C., Faber, S. M., et al. 2022, ApJ, 926, 134
Tacconi, L. J., Genzel, R., & Sternberg, A. 2020, ARA&A, 58, 157
Toft, S., van Dokkum, P., Franx, M., et al. 2007, ApJ, 671, 285
Tortora, C., Napolitano, N. R., Cardone, V. F., et al. 2010, MNRAS, 407, 144
Trujillo, I., Conselice, C. J., Bundy, K., et al. 2007, MNRAS, 382, 109
Valentino, F., Brammer, G., Gould, K. M. L., et al. 2023, ApJ, 947, 20
van der Wel, A., Bell, E. F., Häussler, B., et al. 2012, ApJS, 203, 24
van der Wel, A., Franx, M., van Dokkum, P. G., et al. 2014, ApJ, 788, 28
van der Wel, A., Martorano, M., Haussler, B., et al. 2024, ApJ, 960, 53
van der Wel, A., Rix, H.-W., Wuyts, S., et al. 2011, ApJ, 730, 38
van Dokkum, P. G., Franx, M., Kriek, M., et al. 2008, ApJL, 677, L5
van Dokkum, P. G., Whitaker, K. E., Brammer, G., et al. 2010, ApJ, 709, 1018
Virtanen, P., Gommers, R., Oliphant, T. E., et al. 2020, NatMe, 17, 261
Whitaker, K. E., Ashas, M., Illingworth, G., et al. 2019, ApJS, 244, 16
Whitaker, K. E., van Dokkum, P. G., Brammer, G., et al. 2013, ApJL, 770, L39
Williams, C. C., Giavalisco, M., Bezanson, R., et al. 2017, ApJ, 838, 94
Williams, C. C., Tacchella, S., Maseda, M. V., et al. 2023, ApJS, 268, 64
Williams, R. J., Quadri, R. F., Franx, M., van Dokkum, P., & Labbé, I. 2009, ApJ, 691, 1879
Williams, R. J., Quadri, R. F., Franx, M., et al. 2010, ApJ, 713, 738
Woodrum, C., Williams, C. C., Rieke, M., et al. 2022, ApJ, 940, 39
Wright, L., Whitaker, K. E., Weaver, J. R., et al. 2024, ApJL, 964, L10
Wuyts, S., Förster Schreiber, N. M., van der Wel, A., et al. 2011, ApJ, 742, 96
Xue, Y. Q., Brandt, W. N., Luo, B., et al. 2010, ApJ, 720, 368